buildings

MDPI

Article

A Component Method for Full-Range Behaviour of Embedded Steel Column Bases

Xiaoxu Xu [1,2], Jiafeng Lyu [1,*] and Shen Yan [1,3]

[1] College of Civil Engineering, Tongji University, Shanghai 200092, China; xuxiaoxu@tongji.edu.cn (X.X.); s.yan@tongji.edu.cn (S.Y.)
[2] School of Urban Construction, Hangzhou Polytechnic, Hangzhou 311402, China
[3] State Key Laboratory of Disaster Reduction in Civil Engineering, Tongji University, Shanghai 200092, China
* Correspondence: lyu_jf@tongji.edu.cn

Abstract: This paper introduces a component model for analysing embedded column bases to predict rotational stiffness, moment resistance, and the full-range moment–rotation response. The key components identified include the embedded column, concrete in compression on the column side, concrete in compression beneath the base plate, concrete in punching shear above the base plate, and anchor bolts. The embedded column is modelled as a Timoshenko beam, considering both shear and flexural deformations, while other components are represented by springs. Methods are provided for determining their uniaxial constitutive behaviour. A simplified iterative solution method is proposed, where the embedded column is further simplified into three rigid segments to specifically address shear and bending deformations. A corresponding simplified finite element model is developed for accurate numerical solutions. The validity of the component model is confirmed through comparisons with the results of existing tests and refined solid finite element analysis for H-steel column bases. The simplified iterative solution method effectively predicts strength but underestimates the stiffness of deeply embedded column bases. This is due to the trilinear deformation pattern simplification, which concentrates flexural deformation at the upper bearing stress resultant force point, leading to an overestimation of steel column rotation on the foundation surface.

Keywords: embedded column base; component method; moment–rotation response; initial stiffness; moment resistance

check for updates

Citation: Xu, X.; Lyu, J.; Yan, S. A Component Method for Full-Range Behaviour of Embedded Steel Column Bases. *Buildings* **2024**, *14*, 2337. https://doi.org/10.3390/buildings14082337

Academic Editor: Hiroshi Tagawa

Received: 4 July 2024
Revised: 22 July 2024
Accepted: 26 July 2024
Published: 28 July 2024

Copyright: © 2024 by the authors. Licensee MDPI, Basel, Switzerland. This article is an open access article distributed under the terms and conditions of the Creative Commons Attribution (CC BY) license (https://creativecommons.org/licenses/by/4.0/).

1. Introduction

As a critical component connecting the upper structure and foundation, the column base transmits the axial force, shear force, and moment of the bottom column to the foundation, playing a pivotal role in ensuring the stiffness, strength, and stability of the overall structure. Therefore, the column bases of steel structures are often designed to be fixed and possess greater moment resistance than the plastic moment of the steel column section [1]. Due to higher stiffness, moment resistance, and good ductility compared to exposed column bases and encased column bases, embedded column bases (hereinafter abbreviated as ECBs) are widely utilized in multi-story steel frame structures.

ECBs are typically considered to be fixed due to their substantial stiffness, achieved through sufficient embedded depth. This rigidity often leads to the neglect of their non-rigid behaviours, such as rotation and energy dissipation capacity, in structural analysis. However, recent experimental studies [2] showed that ECBs could exhibit significant flexibility. Under design moments, the rotation of ECBs can reach 0.4% to 0.8% rad. This flexibility may increase the bottom layer's story drift by 20–30% compared to the drift under the assumption of a fixed connection. Inamasu et al. [3,4] found that, at a story drift ratio of 4%, the axial residual deformation of the steel column, taking into account the actual rotation of the ECB, was reduced by 30% to 60% compared to the results under the assumption of a fixed connection. However, this reduction was accompanied by an

increase of 40% to 50% in lateral deformation under the same load. Thus, reasonable utilization of ECB's deformation and rotation can delay local buckling in wide flange columns and reduce axial residual deformation at the same story drift, enhancing seismic resilience and speeding post-disaster repairs. Additionally, for larger steel columns, a deep embedding requirement often results in higher foundation heights, increasing construction costs. Consequently, shallow ECBs with smaller embedded depths have garnered scholarly interest [5]. Cui et al. [6,7] and Richard et al. [8] investigated the hysteretic behaviour of exposed column bases with a floating concrete slab on top (which can be considered shallow ECBs), and significant rotation was observed. Therefore, accurately evaluating the flexural performance of ECBs, including initial stiffness, moment resistance, and full-range behaviour, is crucial for considering the nonlinear interaction between steel columns and foundations in structural analysis.

Considering the non-rigid behaviour of ECBs, recent theoretical research has further explored their flexural behaviour. For the prediction of rotational stiffness, Pecce et al. [9] simplified the sufficiently embedded column to a semi-infinite beam on a Winkler foundation, subjected to shear force and moment, deriving stiffness using the elastic foundation beam theory [10]. However, this model is unsuitable for shallow ECBs as it neglects the effect of embedded depth. The prediction of stiffness is more meaningful for shallow ECBs. Richards et al. [11] treated the embedded column as a finite beam on a Winkler foundation, incorporating the base plate's restraint effect with a bottom rotating spring, but overlooked the base plate's stiffness variation due to embedded depth. Zhao et al. [12] improved Richards' model by modifying the calculation method for rotational stiffness of the base plate to include the influence of embedded depth and taking the shear deformation of the embedded column and the axial force into account. Rodas et al. [13] divided the rotation of the embedded column into two parts: rigid body rotation caused by compression deformation of the concrete on the column side, and column-section rotation at the foundation surface due to bending and shearing of the embedded column. They emphasized that these deformations are determined by the stress distribution characteristics at the limit state.

The prediction of moment resistance initially relied on the findings from joints with similar mechanical behaviour, such as steel coupling beam-to-concrete shear wall joints [14] and through-steel beam-to-precast concrete column joints [15]. The design guidelines and standards such as AIJ [16], AISC 341 [17], and GB 50017 [18] provide theoretical formulas based on the failure mode of concrete crushing outside the column side and the assumption of bearing stress distribution, but tend to be conservative due to ignoring the bending contribution of the base plate. Pertold et al. [19] corrected the amplitude, width, and height of the bearing stress by considering the bearing contribution of concrete between H-steel flanges and the non-uniformity of the compressive stress along the embedded depth. Cui et al. [6] proposed a resistance formula for shallow ECBs that addressed the punching failure of concrete above the base plate and included the base plate's contribution. Richards et al. [11] developed a strength formula based on bolt failure on the tension side, accounting for the overlying slab's role in shifting the compression force centre outward on the base plate. Grilli and Kanvinde [20] proposed a strength model that considered both horizontal and vertical moment-resisting mechanisms. Their model accounts for the influence of embedded depth by introducing the concept of effective embedded depth, limiting the distribution range of bearing stress and incorporating a vertical moment-resisting mechanism contribution coefficient related to embedded depth. Despite these advancements, the model still relies on the failure mode of concrete crushing on the column side.

The aforementioned stiffness and strength models were developed under distinct mechanical models and theoretical frameworks. The stiffness models focused on the deformation coordination between the embedded column and the surrounding concrete, while the strength models were based on specific failure modes and assumed stress distribution patterns. Moreover, different models utilized varying assumptions and parameters, such as the amplitude and distribution range of bearing stress and the degree of the base plate's

contribution to resisting moment. These discrepancies pose challenges in unifying multiple models within a single theoretical framework that encompasses all possible failure modes. The component method [21], however, offers a way to unify the calculation methods for both stiffness and strength.

The component method, introduced in the 1970s–80s [22–24], was later incorporated into the Eurocode for the Design of Steel Structures (Eurocode 3) in the 1990s [25] to determine the mechanical behaviour of structural steel semirigid connections [26]. This method conceptualizes a joint as a system composed of springs and rigid rods, with each spring representing a key component responsible for load transfer within the joint. By describing the stiffness and strength of each component under tension, compression, or shear, the overall stiffness and strength of the joint can be determined by solving the mechanical model. This approach captures all possible failure modes of the joints and the stress states of key components within a unified model. In Eurocode 3 [27], the component method is specifically applied to end-plate connections, including end-plate beam-to-column joints and exposed column bases [28]. Subsequently, the method extended to predict the deformation capacity and full-range behaviour of joints, requiring only the identification of the deformation capacity and full-range behaviour of each component. Its wide application and development potential are evident. Zhu et al. [29] and Wan et al. [30] used the component method to predict the full-range behaviour of beam-to-column joints connected by end-plate and angle steel, respectively. Latour and Rizzano [31] applied the component method to predict the moment–rotation response of exposed column bases. Yan and Rasmussen [32] established an analysis model for steel frames based on the component method, accurately accounting for joint behaviour in advanced steel frame structure analysis. Additionally, numerous studies [33–36] have focused on predicting the full-range behaviour of key components, particularly the equivalent T-stub.

Although the component method has achieved significant success in predicting the stiffness, strength, and full-range behaviour of joints, its application to ECBs has been limited. The primary reasons are: (1) For a considerable period, ECBs were commonly assumed to be fixed. It is only recently that their non-rigid behaviour has garnered significant attention; (2) The component method originated and gained prominence in Europe, where exposed column bases were more frequently adopted than ECBs; (3) Compared to end-plate connections, the mechanical behaviour of ECBs is inherently more complex.

This paper aims to extend the application of the component method to predict the stiffness, strength, and full-range behaviour of ECBs. In Section 2, the moment-resisting mechanisms of the ECB are introduced, and key components are identified and reassembled into a mechanical model consisting of springs and rigid rods. Section 3 details the behaviour of each spring and provides constitutive models. Sections 4 and 5 propose a simplified iterative solution method and a simplified finite element (FE) model based on the component method, respectively. The former avoids complex modelling, while the latter can be applied to advanced analysis of steel frame structures. In Section 6, the validity of the model is verified through the comparison with experimental results and refined solid FE results. Finally, Section 7 summarizes the main contributions and conclusions of this paper.

2. Moment-Resisting Mechanisms and the Component Model

In ECBs, steel columns are directly embedded in reinforced concrete foundations, including independent foundations, raft foundations, and strip foundations. The bottom of the steel column is typically welded to an end plate, which broadens the contact surface between the column's end and the underlying concrete, thereby preventing potential bearing failures. Additionally, the end plate facilitates the installation of anchor bolts to stabilise the steel column during construction. However, in contemporary design practices, the contribution of the end plate to moment-resisting is often disregarded. Consequently, unlike exposed column bases, the anchor bolts in ECBs are usually positioned within the flange. To facilitate the transfer of compression from the column flange to the surrounding

concrete and prevent localized buckling of the web, horizontal stiffeners are installed at the column section near the foundation's surface. In addition to the standard reinforcement within the concrete foundation, vertical reinforcement and stirrups are also positioned around the embedded column. The embedded depth (d_e) and the embedded depth ratio ($\alpha = d_e/h_c$), are critical geometric factors that influence the resistance of ECB. A sufficient embedded depth guarantees the ECB's strength and stiffness, and in China, the embedded depth ratio for H-steel columns must exceed two to ensure a fixed connection [17].

In a steel frame under horizontal load, the ECB experiences not only shear force and moment but also axial force. As shown in Figure 1 and supported by the findings of Kanvinde et al. [2], the moment resistance of the ECB primarily arises from two mechanisms: the horizontal and vertical moment-resisting mechanisms. The deformations of the components induced by these mechanisms are the primary sources of the ECB's rotation.

In the horizontal moment-resisting mechanism, as illustrated in Figure 1a, the concrete on the column side is compressed by the flange, leading to compressive deformation. The compressive stress is distributed on the upper part of one side of the embedded column and the lower part of the opposing side, creating a force couple that counteracts the external moment. Due to the equilibrium of shear forces, the compressive stress on the upper part has a greater magnitude and broader distribution compared to the lower part. Consequently, under the combined effects of moment and shear force, the embedded column exhibits both flexural and shear deformations.

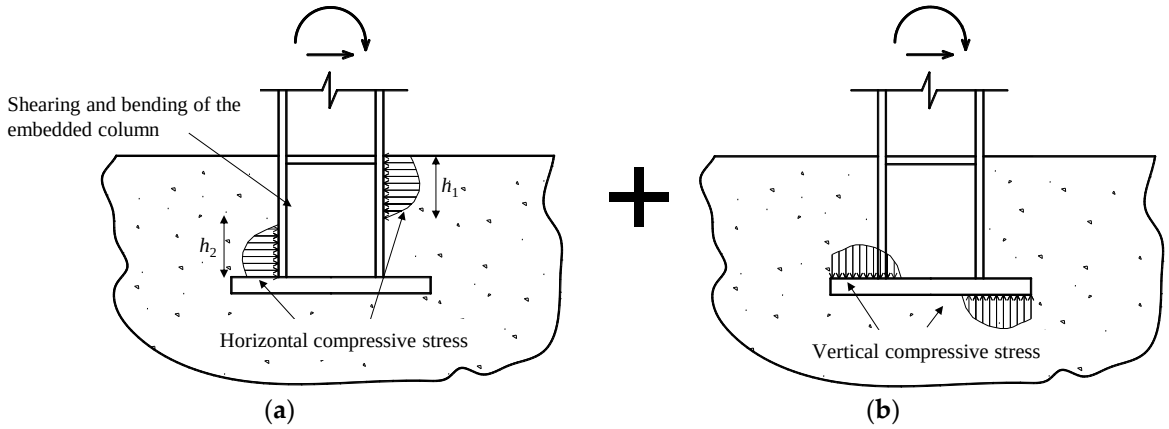


Figure 1. Moment-resisting mechanisms of ECBs [2]. (**a**) Horizontal mechanism; (**b**) vertical mechanism.

As depicted in Figure 1b, the vertical moment-resisting mechanism is provided by the rotational restraint imposed by the surrounding concrete on the base plate. Beneath the base plate, the concrete directly below the column compressive flange undergoes compressive deformation due to the pressure exerted by the base plate. The concrete outside the column tensile flange and above the base plate exhibits uplifting deformation due to the same pressure. The anchor bolts elongate under the tensile force from the base plate, accompanied by the flexural deformation in the base plate itself. Moreover, varying axial forces can create two stress scenarios in the base plate: (1) when the steel column is subjected to large compression, the concrete beneath the base plate undergoes compression, the concrete above the base plate is not uplifted, and the anchor bolts remain unstressed; and (2) when the steel column is subjected large axial tension, the concrete above the base plate exhibits uplifting deformation due to the pressure from the base plate, leading to tensioning of the anchor bolts, and the concrete beneath the base plate remains stress-free.

The moment resistance and stiffness of the ECB increase with the embedded depth due to the significant enhancement of both horizontal and vertical moment-resisting mechanisms. For the horizontal moment-resisting mechanism, greater embedded depth increases the height of compressive stress (specifically, h_1 and h_2 as indicated in Figure 1a) and the moment arm of the force couple. For the vertical mechanism, a deeper embedded depth

enhances the punching shear resistance of the concrete above the base plate. However, the increase in moment resistance and stiffness does not continue indefinitely. The steel column's inherent flexibility limits the effectiveness of deep embedment. As the embedded depth increases, the rotation of the steel column's cross-section diminishes progressively from the foundation's top surface to the base plate. Once the embedded depth surpasses a certain value, the steel column section at the base plate ceases to rotate significantly, making it impossible to form effective vertical moment-resisting mechanisms at the base plate. Grilli and Kanvinde [20] addressed this by introducing the concept of effective depth in their strength model. This model posits that beyond the effective depth, the vertical moment-resisting mechanism's contribution becomes negligible, and horizontal bearing stress is confined to the effective depth range. When evaluating the vertical mechanism's bending contribution for depths shallower than the effective depth, they hypothesize that as the embedded depth increases, the ratio of the moment resistance from the vertical mechanism to joint resistance decreases linearly.

Drawing from the analysis of the moment-resisting mechanisms inherent to ECBs, they can be categorized into distinct force and deformation components. As illustrated in Figure 2a, the horizontal moment-resisting mechanism comprises two primary components: concrete in compression on the column side (ccc) and embedded column in bending and shearing (ecbs). In the vertical moment-resisting mechanism, the key components are concrete in compression beneath the base plate (ccb), concrete in punching shear above the base plate (csb), anchor bolts in tension (bt), and the base plate in bending (bpb).

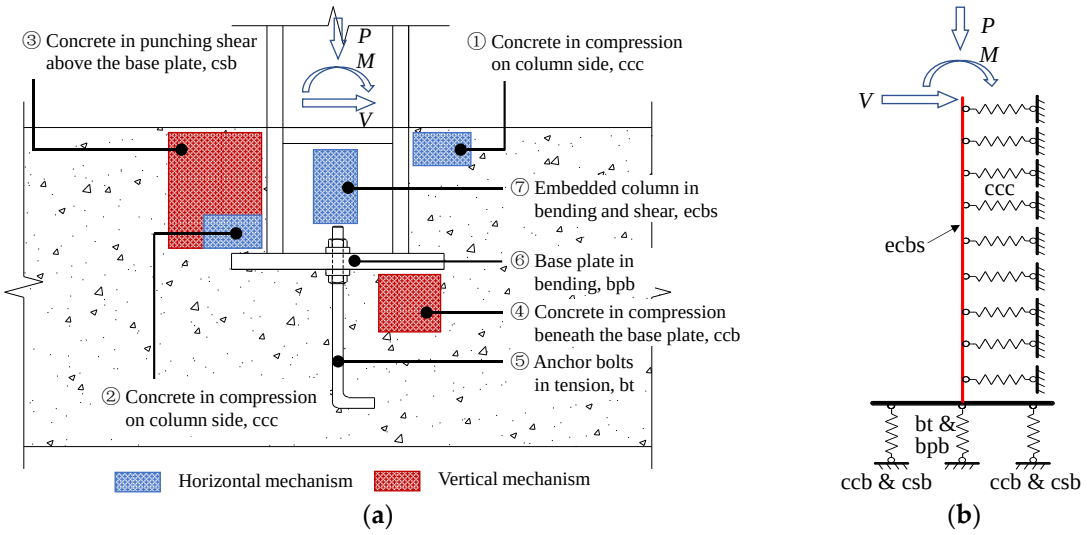


Figure 2. Component identification and assembly of ECBs. (**a**) Component identification; (**b**) component model.

Based on the identification of components, Figure 2b presents an idealized mechanical model. In this framework, component ccc is represented by horizontal springs evenly distributed along the embedded depth on one side, illustrating the nonlinear response of compressive concrete per unit height. The component ecbs is depicted as a Timoshenko beam positioned at the column's axis, incorporating both flexural and shear deformations. The base plate is substituted with a rigid rod, securely fastened to the beam representing the embedded column. The components ccb and csb are denoted by vertical springs centred at the flanges on each side. The components bt and bpb are symbolized by springs at the bolt's axis. Due to the complex interaction between the tensile anchor bolt and the flexural base plate, it is challenging to describe their uniaxial behaviours separately. Following the recommendations of Eurocode 3, they are combined into a spring, with a T-stub method employed to determine their combined uniaxial behaviour. Similarly, due to the complex interaction between the base plate and the bearing concrete, they are equated to a T-stub in

compression to determine uniaxial behaviour. The determination of the load-deformation relationships of these components will be presented in Section 3.

3. Component Behaviour

3.1. Concrete in Compression on the Column Side

The elastic stiffness per unit length (k_e) of the component ccc is calculated by multiplying the foundation coefficient (k_0) by the column width (b_f):

$$k_e = k_0 b_f \tag{1}$$

According to the recommendations of Richards et al. [11], k_0 for the direction along the strong axis of the H-steel column is 41 N/mm^3, while for the direction along the weak axis, k_0 is 54 N/mm^3.

The compressive or tensile strength (F_p) is determined by the following equation:

$$F_p = \beta f_c b_f \tag{2}$$

in which f_c is the concrete compressive strength, and β is a coefficient that accounts for the enhancement effect of the surrounding concrete confinement on the compressive strength. According to the suggestion of Grilli and Kanvinde [20], β is taken as two, as verified by the comparison between the test results and model predictions of ECBs' moment resistances. This value is also consistent with those adopted by Mattock and Gaafar [37], Deierlein et al. [38], and Sheikh et al. [39], and it has subsequently been codified in the ASCE Guidelines for composite connections [40].

The stiffness and strength of the compressive concrete per unit length are given by Equations (1) and (2), respectively. However, there is currently no available reference for the full-range load–displacement relationship. Here, referring to the form of the uniaxial compressive constitutive model of concrete, it is assumed that the load–displacement relationship of component ccc follows the same form. The Hogenestad model, which is adopted by concrete design codes in countries such as China, Europe, and the United States, is shown in Figure 3a. The ascending segment is a quadratic function, and the descending segment is a linear function. Its expression is as follows:

$$\sigma = \begin{cases} \left[2\frac{\varepsilon}{\varepsilon_p} + \left(\frac{\varepsilon}{\varepsilon_p}\right)^2\right] f_c & 0 \le \varepsilon < \varepsilon_p \\ \left(1 - 0.15\frac{\varepsilon - \varepsilon_p}{\varepsilon_u - \varepsilon_p}\right) f_c & \varepsilon_p \le \varepsilon < \varepsilon_u \end{cases} \tag{3}$$

in which ε_p and ε_u are the peak strain and ultimate strain, respectively. For C30 concrete, ε_p and ε_u are typically taken as 0.002 and 0.0038, respectively [41]. By derivation, it can be understood that the secant modulus at the peak point is twice the initial stiffness, i.e., $\varepsilon_p = 2f_c/E_c$, where E_c is the concrete modulus. Many uniaxial stress–strain models for concrete adopt the form of the Hogenestad model. For instance, both the Concrete01 and Concrete02 constitutive models widely used in OpenSees 3.6.0 [42] employ the Hogenestad curve for the ascending segment, with a straight line for the descending segment. When the strain exceeds ε_u, the stress is equal to the ultimate strength.

This assumes that the ascending segment of the load–displacement relationship of the concrete per unit length is the same as the Hogenestad model, which is a quadratic function, while the descending segment is a straight line. When the displacement exceeds the ultimate displacement Δ_u, the load is equal to the ultimate strength F_u. The expression is as follows:

$$F = \begin{cases} F_p \frac{\Delta}{\Delta_p}\left(2 + \frac{\Delta}{\Delta_p}\right) & 0 \le \Delta < \Delta_p \\ F_p + \frac{F_u - F_p}{\Delta_u - \Delta_p}(\Delta - \Delta_p) & \Delta_p \le \Delta < \Delta_u \\ F_u & \Delta \ge \Delta_u \end{cases} \tag{4}$$

in which Δ_p is the peak displacement which is equal to $2F_p/k_e$.

For ease of application, the load–displacement curve is simplified into a four-linear curve, as shown in Figure 3b. According to the principle of energy equivalence, the elastic limit F_e is taken as $2/3F_p$, and the corresponding plastic stiffness k_p is equal to $1/4k_e$. Referring to the concrete constitutive model, Δ_u and F_u are equal to $1.9\Delta_p$ and $0.85F_p$, respectively. Additionally, since uniformly distributed springs placed on one side are used to represent the compressive behaviour of the concrete on both sides of the column, the full-range tension-compression behaviour of the springs can ultimately be represented by the curve shown in Figure 4.

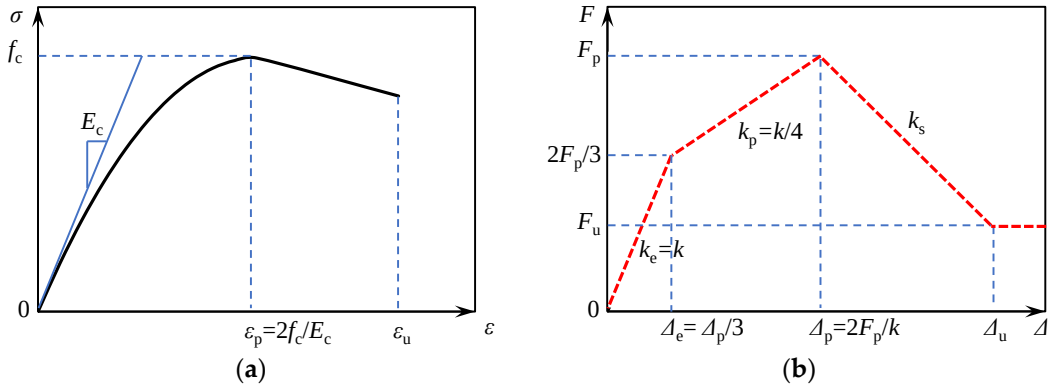


Figure 3. Concrete constitutive and compressive behaviour of the component ccc. (**a**) Compressive constitutive of concrete; (**b**) compressive behaviour of the component ccc.

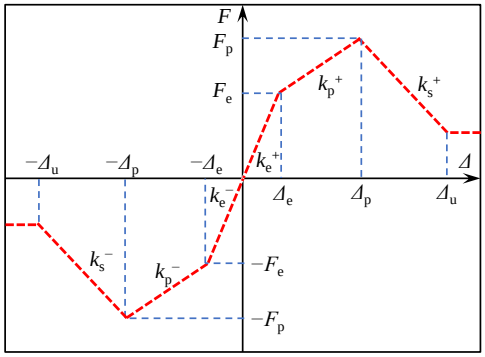


Figure 4. Full-range load–displacement curve of the component ccc.

3.2. Concrete in Compression Beneath the Base Plate

The initial compressive stiffness (k_e^-) and peak strength (F_p^-) of the component ccb can be determined based on the method for the behaviour of equivalent T-stub in compression codified in Eurocode 3 [27]. Due to the flexibility of the base plate, the compressive stress is concentrated in the area near the column section. Stockwell [43] proposed replacing the flexible base plate with uneven stress distribution with an equivalent rigid plate with uniform stress distribution. As shown in Figure 5, considering stress diffusion, the concrete compression area beneath the base plate of the H-steel column is divided into three rigid rectangular areas, which can be regarded as three equivalent T-stubs and represented by three compression-only springs beneath the base plate.

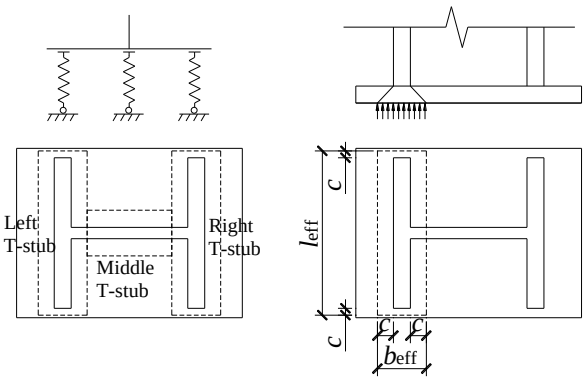


Figure 5. Equivalent T-stub in compression.

The compressive strength of the equivalent T-stub in compression is calculated by:

$$F_{\mathrm{p}}^{-} = f_{\mathrm{j}} b_{\mathrm{eff}} l_{\mathrm{eff}} \tag{5}$$

$$f_{\mathrm{j}} = \beta_{\mathrm{j}} k_{\mathrm{j}} f_{\mathrm{c}} \tag{6}$$

in which b_{eff} and l_{eff} are the effective width and effective length of the equivalent T-stub, respectively. For an equivalent T-stub composed of a column flange and a base plate, $b_{\mathrm{eff}} = t_{\mathrm{f}} + 2c$ and $l_{\mathrm{eff}} = b_{\mathrm{f}} + 2c$, where c is the stress diffusion width and t_{f} is the flange thickness. For an equivalent T-stub composed of a column web and a base plate, $b_{\mathrm{eff}} = t_{\mathrm{w}} + 2c$ and $l_{\mathrm{eff}} = h_{\mathrm{c}} - 2t_{\mathrm{f}} - 2c$, where t_{w} is the web thickness and h_{c} is the column height. If the calculated results exceed the range of the base plate, only the area within the base plate range is effective. f_{j} is the compressive strength of the concrete in the rigid region. k_{j} is a concentration factor reflecting the edge effect, and the specific calculation method is shown in Figure 6. When the base plate is sufficiently far from the edge of the concrete foundation, $k_{\mathrm{j}} = 5$. β_{j} is a reduction factor considering the quality of the bedding grouting. When the characteristic strength of the bedding is greater than 0.2 times the characteristic strength of the concrete and the thickness of the bedding is less than 0.2 times the minimum width of the base plate, $\beta_{\mathrm{j}} = 2/3$. If these conditions are not met, the performance of the bedding needs to be evaluated separately. c is determined based on the condition that the base plate just reaches bending yield under the compressive stress f_{j}, i.e., $1/2 f_{\mathrm{j}} c^2 = 1/6 {t_{\mathrm{p}}}^2 f_{\mathrm{y}}$, in which f_{y} is the yield strength of the base plate and t_{p} is the thickness of the base plate. Then,

$$c = t_{\mathrm{p}} \sqrt{\frac{f_{\mathrm{y}}}{3 f_{\mathrm{j}}}} \tag{7}$$

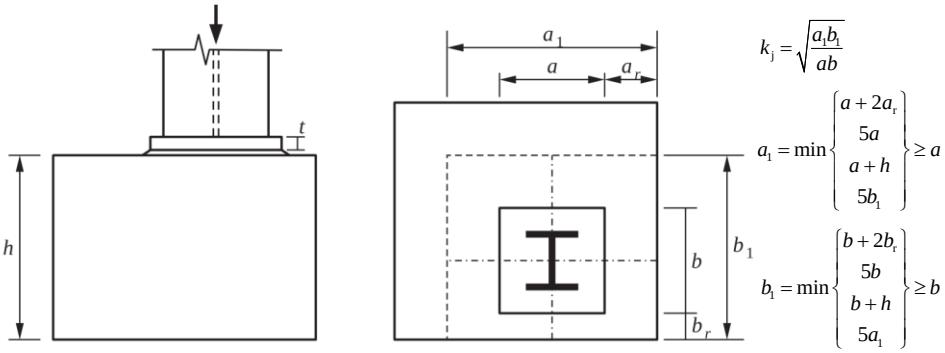


Figure 6. Concentration factor reflecting the edge effect [27].

The compressive stiffness of the equivalent T-stub in compression is calculated using Equation (8). The specific derivation process can be found in reference [44].

$$k_e^- = \frac{E_c\sqrt{b_{eff}l_{eff}}}{1.275} \tag{8}$$

in which E_c is the elastic modulus of concrete, which can be calculated according to ACI 318 [42] using the formula $E_c = 4700\sqrt{f_c}$.

Assuming that the compressive behaviour of the equivalent T-stub also follows the aforementioned four-linear model and that this component cannot withstand tensile forces, the full-range load–displacement relationship is shown in Figure 7. The coordinates of the characteristic points are $(-\Delta_e, -F_e) = (-2F_p^-/(3k_e^-), -2F_p^-/3)$, $(-\Delta_p, -F_p) = (-2F_p^-/k_e^-, -F_p^-)$, and $(-\Delta_u, -F_u) = (-3.8F_p^-/k_e^-, 0.85F_p^-)$.

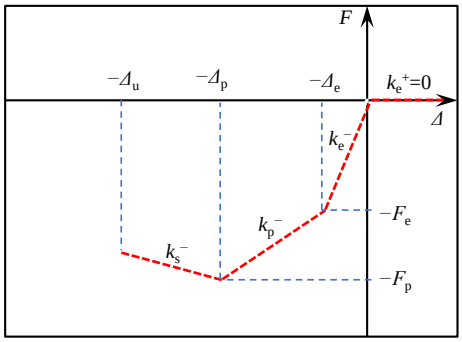


Figure 7. Full-range load–displacement curve of the component ccb.

3.3. Concrete in Punching Shear above the Base Plate

Referring to the formula for the punching shear strength of concrete slabs with stirrup provided by ACI 318 [45] under local load or concentrated reaction force, the punching shear strength of the concrete above the base plate can be calculated by:

$$F_p = F_{c,p} + F_{s,p} = 0.5 \times 0.33\sqrt{f_c}u_m h_0 + f_{yv}A_{svu} \tag{9}$$

in which $F_{c,p}$ and $F_{s,p}$ represent the contributions of concrete and stirrup, respectively; h_0 is the distance from the upper surface of the base plate to the foundation surface, i.e., $h_0 = d_e - t_p$; f_{yv} is the yield strength of the vertical reinforcement around the column; A_{svu} is the total area of all vertical reinforcement intersecting with the 45° punching shear failure cone; and u_m is the calculated perimeter, taken as the average of the top and bottom perimeters of the punching shear failure cone. Influenced by the foundation width (B_c), two possible failure surfaces for punching shear can occur, as shown in Figure 8. The smaller calculated perimeter of the two punching shear failure surfaces is taken as u_m:

$$u_m = \min\left(2b_p + h_p - h_c - b_c + \pi h_0,\ 2B_c - b_c\right) \tag{10}$$

in which b_c and h_p are the width and height of the base plate.

For the initial stiffness, Zhao et al. [12] simplified the concrete block subjected to the uplifting effect of the base plate on the tensile flange side as an equivalent simply supported beam, as shown in Figure 9. Here, L represents the equivalent beam length, L_{ct} represents the distance between the mid-surfaces of the flanges on both sides of the steel column, and the equivalent beam width is taken as the column width b_c. Considering shear and flexural deformations, the initial stiffness can be calculated by:

$$k_e = \frac{1}{\frac{LL_{ct}^2}{3E_cI}\left(1 - \frac{L_{ct}}{L}\right)^2 + \frac{L_{ct}}{\mu G_c A}\left(1 - \frac{L_{ct}}{L}\right)} \tag{11}$$

in which E_cI and μGA represent the flexural stiffness and shear stiffness of the equivalent beam, respectively.

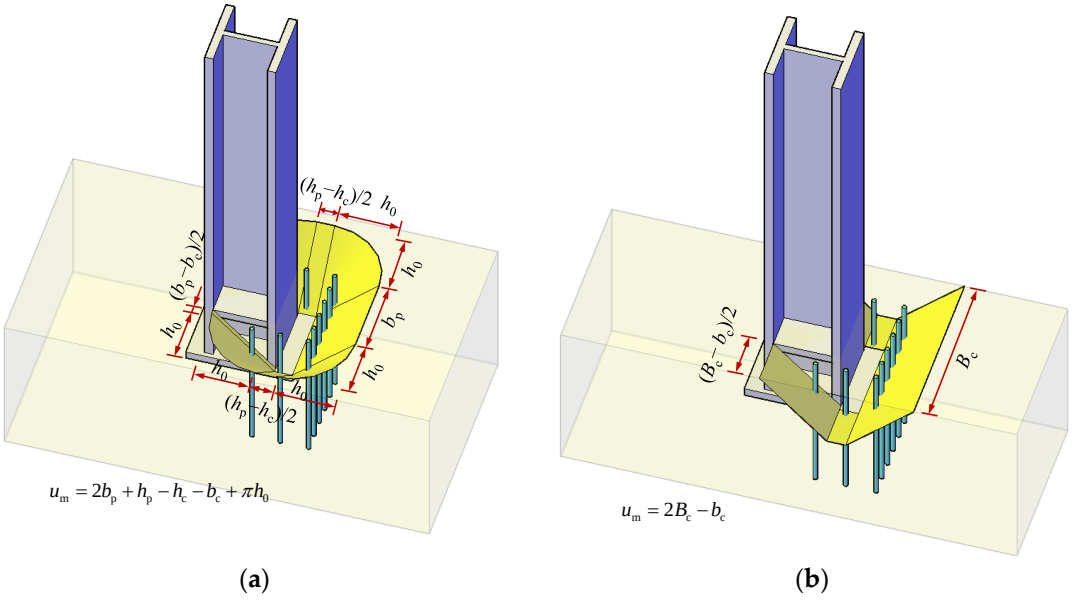


Figure 8. Failure surfaces of the concrete in punching shear above the base plate. (**a**) Punching shear surface I; (**b**) punching shear surface II.

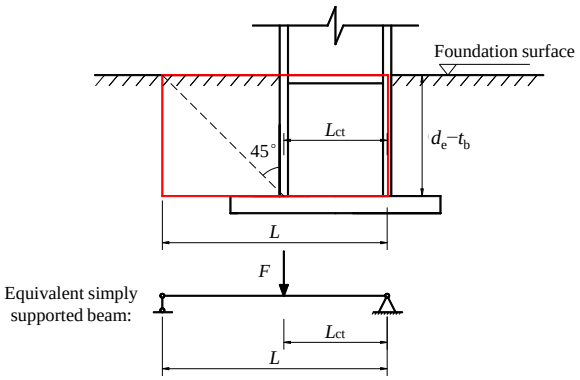


Figure 9. Equivalent beam model for the stiffness prediction of the component csb [12].

When the component csb is equivalent to an axial spring located below the base plate, the spring can only withstand tension but not compression and its tensile load–displacement curve is simplified as a trilinear model, as shown in Figure 10. The trilinear model consists of an elastic segment, a softening segment, and a post-softening plateau segment. The strength and stiffness of the elastic segment have been given by Equations (9) and (11); the stiffness of the softening segment is $\gamma_s k_e$, where γ_s is the tensile softening modulus, taken as −0.1 [41]. As the displacement increases, the punching resistance provided by the concrete gradually diminishes. The ultimate strength F_u, corresponding to the post-softening plateau segment, is only provided by the steel rebars, so is equal to $f_{yv}A_{svu}$.

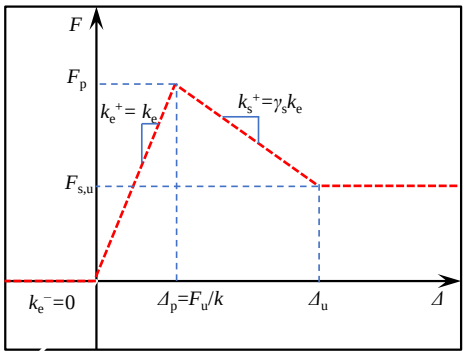


Figure 10. Full-range load–displacement curve of the component csb.

3.4. Anchor Bolt in Tension

Eurocode 3 [27] idealises the anchor bolts and base plate as an equivalent T-stub in tension through the equivalent length method to calculate the stiffness (k_e) and strength (F_p). The specific method for determining the effective length (l_{eff}) can be found in Eurocode 3. The tensile strength of the equivalent T-stub is the minimum strength related to all possible failure modes as illustrated in Figure 11a, and is calculated by:

$$F_p = \begin{cases} \min\left(\frac{4M_p}{m}, \frac{2M_p+2B_u n}{m+n}, 2B_u\right) & L_b \le \frac{8.8m^3A_b}{l_{eff}t_p^3} \\ \min\left(\frac{2M_p}{m}, 2B_u\right) & L_b > \frac{8.8m^3A_b}{l_{eff}t_p^3} \end{cases} \quad (12)$$

in which the three terms in the first function min() correspond to three typical failure modes when there is a prying force, while the two terms in the second function min() correspond to two typical failure modes when there is no prying force, as shown in Figure 11a; M_p ($=f_y l_{eff} {t_p}^2/4$) is the plastic moment of the base plate section within the effective length; B_u is the tensile strength of the anchor bolts; A_b is the cross-sectional area of the anchor bolts; L_b is the effective length of the anchor bolts, taken as eight times the diameter of the anchor bolts plus the total thickness of the grouting layer, base plate and washer, as well as half the height of the nut and bolt head; and parameters m and n are geometric parameters, and their values can be referenced in Eurocode 3.

The initial stiffness of the equivalent T-stub in tension is calculated by the series superposition of the flexural stiffness of the flange and the tensile stiffness of the bolts:

$$k_e = \begin{cases} \left(\frac{m^3}{0.85El_{eff}t_p^3} + \frac{L_b}{1.6EA_b}\right)^{-1} & L_b \le \frac{8.8m^3A_b}{l_{eff}t_p^3} \\ \left(\frac{m^3}{0.425El_{eff}t_p^3} + \frac{L_b}{2EA_b}\right)^{-1} & L_b > \frac{8.8m^3A_b}{l_{eff}t_p^3} \end{cases} \quad (13)$$

Although Eurocode 3 provides methods for determining the initial stiffness and strength of equivalent T-stubs, it does not explicitly specify how to determine their full-range behaviour based on the strength and stiffness. Fortunately, Eurocode 3 provides recommendations for determining the moment–rotation curves of end-plate connections, including exposed column bases and beam-to-column connections: Clause 6.3.1(6) states that when the moment exceeds 2/3 of the joint's resistance, the joint's response becomes nonlinear, and the secant stiffness at the peak strength is 1/3 of the initial stiffness. This prediction model is supported by the results of bending tests on end-plate connections [46,47]. On the other hand, the test results of end-plate connections also indicate that the bending end-plate and column flange, which can be equivalent to T-stubs, are the primary source of rotational deformation in the joint [47,48], so that the last 1/3 of the T-stub's response before the peak is nonlinear, with secant stiffness at peak being 1/3 of the initial stiffness. This implies a post-yield stiffness of 1/7 of the initial stiffness. Therefore, the tensile load–displacement response of the equivalent T-stub can be represented by the trilinear model

as shown in Figure 11b. This model applies to T-stubs that experience flange yielding and has been verified against the tests on bolted T-stubs with various yield line patterns [33,49], although it provides relatively conservative estimates for ultimate resistance. In cases of anchor bolt fracture, where the flange does not exhibit significant plastic deformation and the deformation is primarily concentrated in the tensile deformation of the anchor bolt, the plastic capacity is reached when the load attains the yield strength of the anchor bolt. Hence, a bilinear ideal elastoplastic model is used to describe its stress behaviour. Additionally, when the base plate and anchor bolts are under compression, the pressure is directly transmitted to the foundation concrete through the bearing action between the base plate and the concrete. Therefore, the compressive behaviour can be neglected.

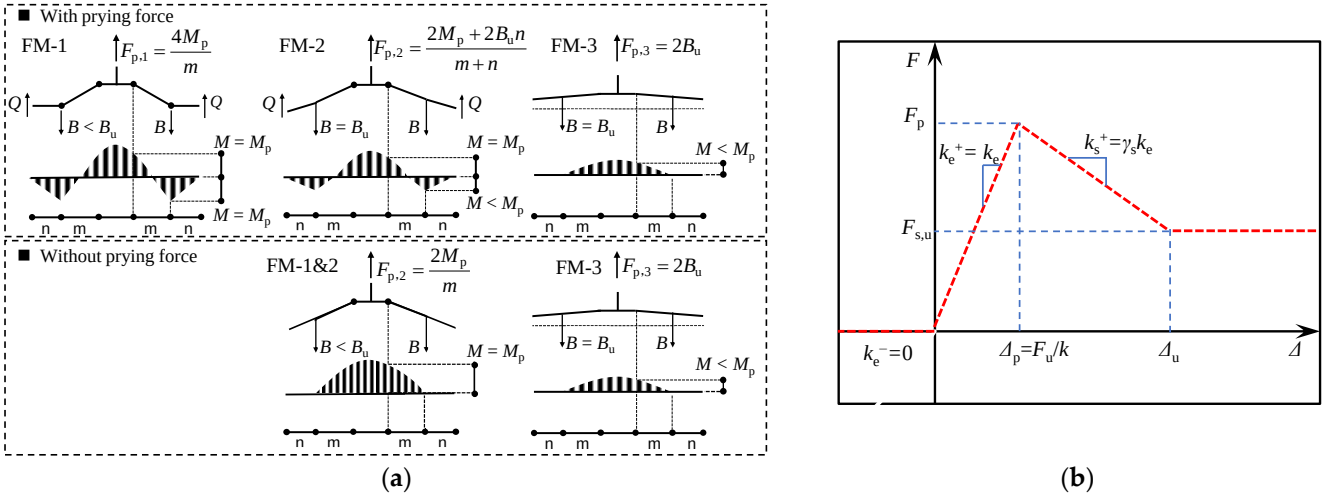


Figure 11. Equivalent T-stub in tension. (**a**) Force diagram; (**b**) full-range load–displacement curve.

3.5. Summary of Basic Components

Table 1 summarizes the uniaxial load–displacement relationships of the four basic components mentioned above.

Table 1. Summary of basic components.

F-Δ Curves	Equations	*F*-Δ Curves	Equations
1 Concrete in compression on the column side	$F_e^+ = -F_e^- = 2F_p/3$ $F_p^+ = -F_p^- = \beta f_c b_f$ $F_u^+ = -F_u^- = 0.85F_p^+$ $k_e^+ = k_e^- = k_0 b_f$ $k_p^+ = k_p^- = 0.25k_e^+$ $k_s^+ = k_s^- = -0.083k_e^+$	2 Concrete in compression beneath the base plate (T-stub in compression)	$F_e^- = 2F_p^-/3$ $F_p^- = -f_j b_{eff} l_{eff}$ $F_u^- = 0.85F_p^-$ $k_e^- = \frac{E_c\sqrt{b_{eff}l_{eff}}}{1.275}$ $k_p^- = 0.25k_e^-$ $k_s^- = -0.083k_e^-$

Table 1. *Cont.*

F-Δ Curves	Equations	*F*-Δ Curves	Equations
3 Concrete in punching shear above the base plate	$F_p^+ = 0.5 f_t u_m h_0 + 0.8 f_{yv} A_{svu}$ $F_u^+ = 0.8 f_{yv} A_{svu}$ $k_e^+ = \frac{1}{\frac{L^3\alpha^2(1-\alpha)^2}{3EI} + \frac{L\alpha(1-\alpha)}{\mu GA}}$ $k_s^+ = -0.1 k_e^+$ $\alpha = \frac{L_{ct}}{L}$	4 Anchor bolt in tension(T-stub in tension)	$F_e^+ = 2F_p^+/3; k_p^+ = k_e^+/7$ $F_{p,1}^+ = \min\left(\frac{2M_p}{m}, \frac{2M_p+2B_u n}{m+n}, 2B_u\right)$ $F_{p,2}^+ = \min(2M_p/m, 2B_u)$ $k_{e,1}^+ = \left(\frac{m^3}{0.85 E l_t t_f^3} + \frac{L_b}{1.6 E A_b}\right)^{-1}$ $k_{e,2}^+ = \left(\frac{m^3}{0.425 E l_t t_f^3} + \frac{L_b}{2 E A_b}\right)^{-1}$ $F_p^+ = \begin{cases} F_{p,1}^+ & L_b \le L_{b,m} \\ F_{p,2}^+ & L_b > L_{b,m} \end{cases}$ $k_e^+ = \begin{cases} k_{e,1}^+ & L_b \le L_{b,m} \\ k_{e,2}^+ & L_b > L_{b,m} \end{cases}$ $L_{b,m} = 8.8 m^3 A_b / \left(l_{eff} t_p^3\right)$

When different components can be represented by springs located at the same position below the base plate, the behaviour of these components can be combined. For example, the components csb and ccb (on the flange side) can be represented by a spring with tension-compression asymmetric behaviour located below the flange. Similarly, the anchor bolt located in the middle of the base plate and the component ccb (on the web side) can also be represented by a spring with tension-compression asymmetric behaviour located below the web. Figure 12 shows the component models for ECBs with different configurations of the base plate and the constitutive models of the equivalent springs.

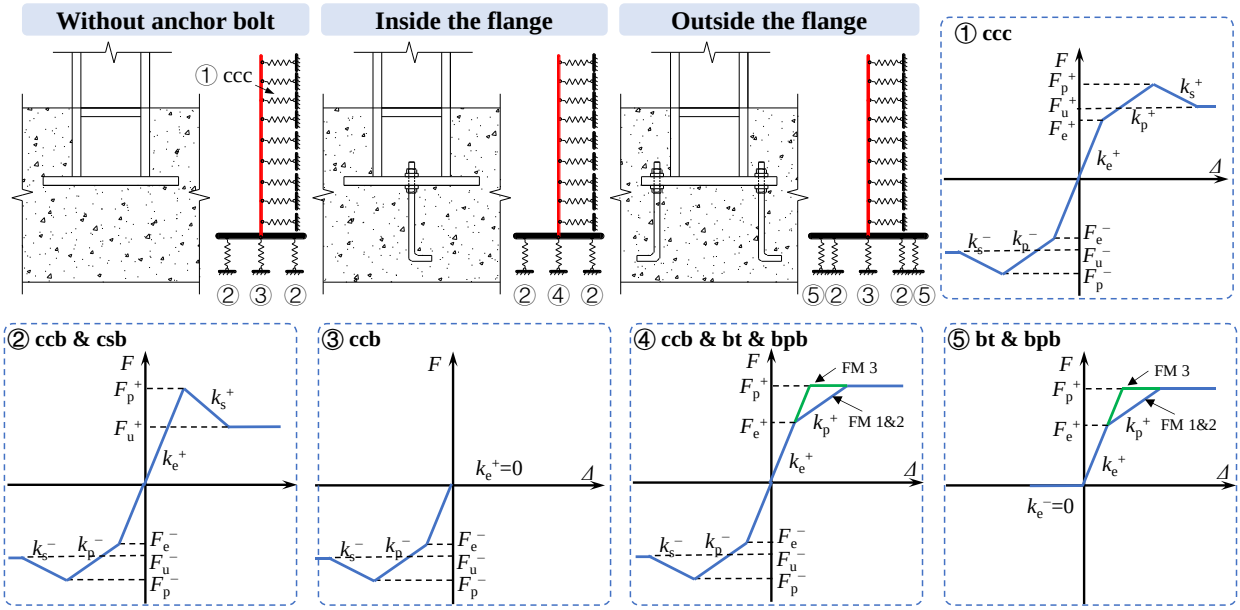


Figure 12. Component models for ECBs with different configurations of the base plate.

4. Solution of Full-Range *M*-*θ* Curve—Simplified Method

4.1. Simplified Model

Due to the complex nonlinear behaviour of springs and the intricate deformation coordination relationships among various components, the mechanical models shown in Figures 2 and 12 are difficult to solve unless numerical calculation methods such as FE analysis are employed, which will be presented in Section 5. Therefore, this paper proposes a simplified method for solving the system response.

As shown B in Figure 13, the distributed bearing stress on both sides of the embedded column can be equated to two concentrated forces. The upper concentrated force acts at the position where the moment in the cross-section is maximum; hence, it is assumed that the bending deformation is concentrated at this position. The shear force in the cross-section between the upper and lower concentrated forces is maximum and constant, so it is assumed that the shear deformation occurs uniformly between the two concentrated forces. Finally, as shown C in Figure 13, the embedded column is divided into three segments based on the positions of the equivalent concentrated forces. Each segment is represented by a rigid rod, and relative rotation can occur between them. The bending and shear deformations of the embedded column are concentrated and represented at the rotation points. As shown in E in Figure 13, the difference between the rotation θ_t of segment I and the rotation θ_b of segment III, i.e., θ_t- $-$ θ_b, represents the difference in rotation at the two ends due to bending deformation. The relative rotation $\theta_b - \theta_0$ between segments III and II represents the rotation of the column's central axis caused by shear deformation. Therefore, the relative rotation $\theta_t - \theta_0$ between segments I and II is the sum of the rotation caused by both bending and shear deformations.

The restraint moment generated by the base plate is only related to the rotation of the base plate and the constitutive models of the vertical springs representing the vertical moment-resisting mechanism. Therefore, as shown in D in Figure 13, the rigid rod representing the base plate and the vertical springs can be first equivalent to a nonlinear rotational spring to achieve further simplification.

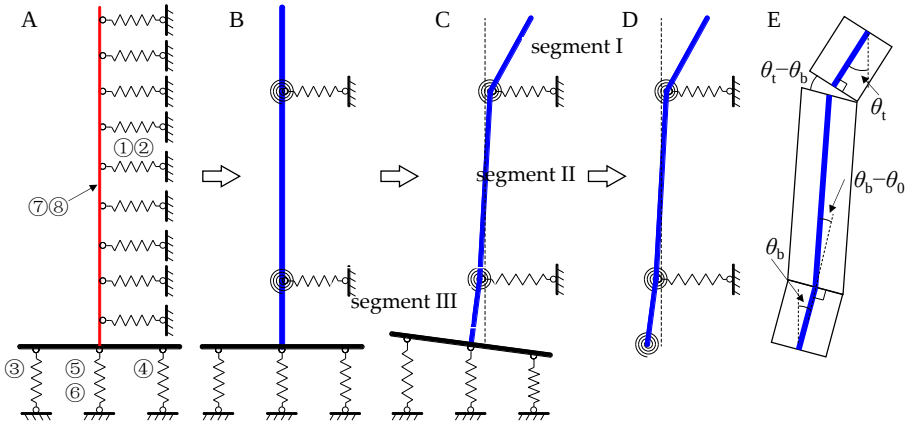


Figure 13. Simplification of the component model.

4.2. Moment–Rotation Curves of the Base Plate

Under the moment M_b and axial force P, the deformation of the base plate is uniquely determined by rigid-body axial displacement and rotation around a certain point, as shown in Figure 14b. Theoretically, this point can be located anywhere, but for the convenience of establishing equations, the intersection point of the neutral axis of the steel column and the base plate is chosen. Denoting the rigid-body displacement and rotation as δ_b and θ_b, respectively, and the springs from right to left as s_1, s_2, …, with the vertical distance from spring s_i to the neutral axis being h_i, the axial deformation of spring s_i (tension is positive) is:

$$\delta_i = \delta_b + \theta_b h_i \tag{14}$$

The spring's load–displacement curve is represented by a multi-linear model and linear interpolation is used to obtain the internal force of the spring:

$$F_i = f(\delta_i) \tag{15}$$

The springs' forces satisfy both the following axial equilibrium equation and the rotational equilibrium equation:

$$P + \sum F_i = 0 \tag{16}$$

$$M_b = \sum F_i h_i \tag{17}$$

In theory, by Equations (16) and (17), the values of δ_b and θ_b can be obtained. However, since Equation (15) is a piecewise linear function, it is inconvenient to derive analytical expressions for δ_b and θ_b. Therefore, an easily implementable and convergent iterative solution method is proposed here, and the flowchart is shown in Figure 15:

1. First, an arbitrary value of θ_b is given and δ_b is assumed to be 0;
2. Calculate F_i and the tangent stiffness k_i of the spring by Equations (15) and (18); k_i is also a piecewise linear function of the spring's deformation δ_i;

$$k_i = g(\delta_i) \tag{18}$$

3. Judge whether the axial equilibrium, i.e., Equation (16), is satisfied. If not, obtain a new value for δ_b by Equation (19), then return to step 1 and solve for the new values of F_i and k_i until Equation (16) is satisfied;

$$\delta_b = \frac{-P - \sum F_i}{\sum k_i} \tag{19}$$

4. Calculate M_b by Equation (17). Thus far, a point (θ_b, M_b) on the moment–rotation curve of the base plate has been obtained;
5. Gradually increase θ_b and solve for a series of points to obtain the full moment–rotation curve of the base plate. The precision of the moment–rotation curve of the base plate depends on the precision of the component behaviour description and the magnitude of the θ_b increment given during the solution process.

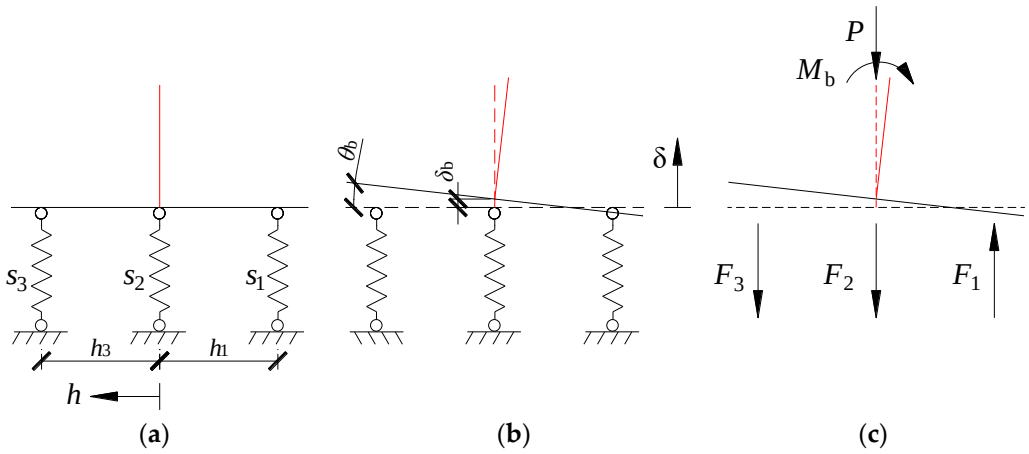


Figure 14. Mechanical model and force diagram of the base plate. (**a**) Mechanical model; (**b**) deformation mode; (**c**) force diagram.

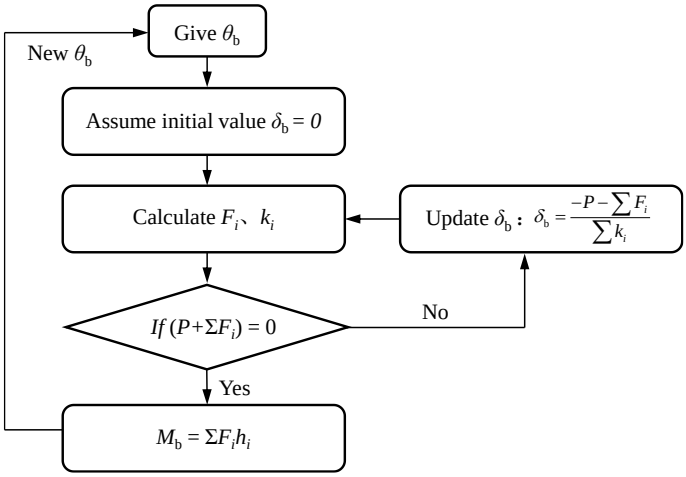


Figure 15. Flowchart for obtaining the moment–rotation curve of the base plate.

4.3. Mechanical Model

As shown in Figure 16, determining the deformation of the embedded column under any load (M, V, with the relationship $M = V \cdot L_c$, where L_c is the height of the inflection point) requires six geometric parameters, including the rotation θ_t of segment I, the rotation θ_0 of segment II, the rotation θ_b of segment III, the distance d_t from the bearing stress reversal point (i.e., point B, where the bearing stress or lateral deformation is 0) to the foundation surface, the distance D_t from the upper equivalent concentrated force action point (point A) to the bearing stress reversal point, and the distance D_b from the lower equivalent concentrated force action point (point C) to the bearing stress reversal point.

Determining the internal force of the ECB requires three force parameters: the restraining moment M_b provided by the base plate, the upper equivalent concentrated force P_t, and the lower equivalent concentrated force P_b.

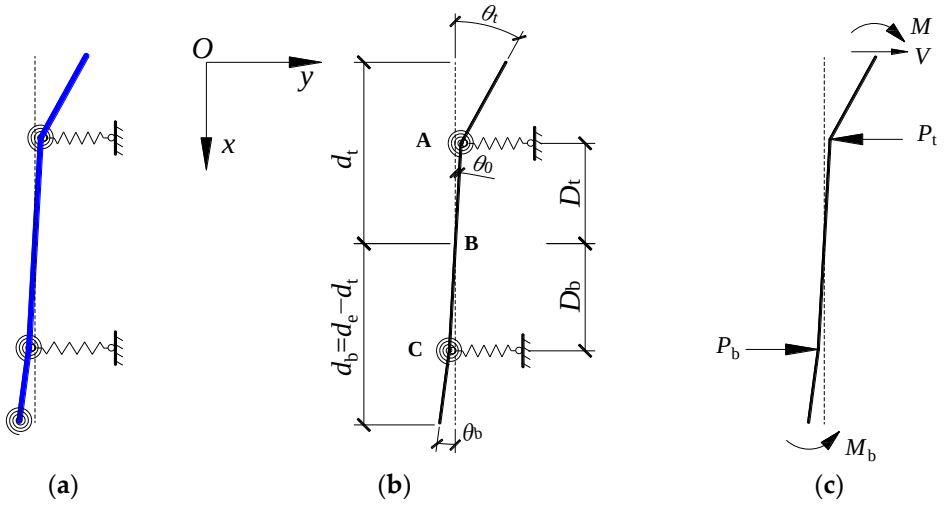


Figure 16. Mechanical model and force diagram of the ECB. (**a**) Component model; (**b**) geometric dimensions and deformation modes; (**c**) force diagram.

The external loads M and V, along with the foundation reactions M_b, P_t, and P_b, must satisfy the following equilibrium equations:

$$P_t - P_b - \frac{M}{L_c} = 0 \tag{20}$$

$$M_b + P_b(d_t + D_b) - P_t(d_t - D_t) - M = 0 \tag{21}$$

$$\int_0^{d_t} p(x)dx = P_t \tag{22}$$

$$\int_0^{d_t} p(x)xdx = P_t(d_t - D_t) \tag{23}$$

$$\int_{d_t}^{d_e} p(x)dx = -P_b \tag{24}$$

$$\int_{d_t}^{d_e} p(x)xdx = -P_b(d_t + D_b) \tag{25}$$

in which $p(x)$ represents the distributed force provided by the distributed springs, which is uniquely determined by the lateral displacement $y(x)$ calculated using the geometric parameters θ_t, θ_0, θ_b, d_t, D_t, D_b, and the constitutive relationship of the distributed springs:

$$y(x) = \begin{cases} \theta_0 D_t + \theta_t(d_t - D_t - x) & x \le d_t - D_t \\ \theta_0(d_t - x) & d_t - D_t < x \le d_t + D_b \\ -\theta_0 D_b + \theta_b(d_t + D_b - x) & d_t + D_b < x \end{cases} \tag{26}$$

$$p(x) = \begin{cases} k_1 y(x) + \sum_{i=1}^{n} (k_{i+1} - k_i)(y - \Delta_i) \cdot H(y - \Delta_i) & y \ge 0 \\ k_1 y(x) + \sum_{i=1}^{n} (k_{i+1} - k_i)(y + \Delta_i) \cdot H(-y - \Delta_i) & y < 0 \end{cases} \tag{27}$$

in which $H(x)$ is the Heaviside function; k_i is the slope of the ith segment of the multi-linear constitutive model, and Δ_i is the deformation corresponding to the end of the ith segment; n equals the number of segments minus 1; and the origin position and positive direction of the coordinates x and y refer to Figure 16. Specifically, corresponding to the constitutive model of the component ccc, n = 3; k_1, k_2, k_3, $k_4 = k_e$, k_p, k_s, 0; and Δ_1, Δ_2, $\Delta_3 = \Delta_e$, Δ_p, Δ_u.

Substituting Equations (26) and (27) into Equations (22) to (25), the simplified forms can be obtained:

$$\begin{aligned} P_j = {} & \frac{1}{2}k_1\theta_0 d_j^2 + \frac{1}{2}k_1(\theta_j - \theta_0)(d_j - D_j)^2 \\ & + \frac{\theta_0}{2}\sum_{i=1}^{n}(k_{i+1} - k_i)(D_j - D_{i,0})^2 \cdot H(D_j - D_{i,0}) \\ & + \frac{\theta_j}{2}\sum_{i=1}^{n}(k_{i+1} - k_i)(d_j - D_j)(d_j + D_j - 2D_{i,0}) \cdot H(D_j - D_{i,j}) \\ & + \frac{\theta_j}{2}\sum_{i=1}^{n}(k_{i+1} - k_i)(d_j - D_{i,j})^2 \cdot H(-D_j + D_{i,j}) \cdot H(d_j - D_{i,j}) \end{aligned} \tag{28}$$

$$\begin{aligned} P_j D_j = {} & \frac{1}{3}k_1\theta_0 d_j^3 + \frac{1}{6}k_1(\theta_j - \theta_0)\left(2d_j^3 - 3d_j^2 D_j + D_j^3\right) \\ & + \frac{\theta_0}{6}\sum_{i=1}^{n}(k_{i+1} - k_i)\left(2D_j^3 - 3D_j^2 D_{i,0} + D_{i,0}^3\right) \cdot H(D_j - D_{i,0}) \\ & + \frac{\theta_j}{6}\sum_{i=1}^{n}(k_{i+1} - k_i)\left(2d_j^3 - 3d_j^2 D_{i,j} + 3D_j^2 D_{i,j} - 2D_j^3\right) \cdot H(D_j - D_{i,j}) \\ & + \frac{\theta_j}{6}\sum_{i=1}^{n}(k_{i+1} - k_i)\left(2d_j^3 - 3d_j^2 D_{i,j} + D_{i,j}^3\right) \cdot H(-D_j + D_{i,j})H(d_j - D_{i,j}) \end{aligned} \tag{29}$$

in which:

$$D_{i.0} = \frac{\Delta_i}{\theta_0};\ D_{i,j} = \frac{\Delta_i + (\theta_j - \theta_0)D_j}{\theta_j} \tag{30}$$

where the subscript j represents t or b.

The restraining moment M_b provided by the base plate and the rotation θ_b satisfy the moment–rotation relationship of the base plate obtained in Section 4.2:

$$M_b = f(\theta_b) \tag{31}$$

The difference in rotation between segments I and III, i.e., $\theta_t - \theta_b$, is equal to the difference in rotation at the two ends of the beam under the action of external loads M, V, and foundation reaction forces M_b, P_t, P_b, which corresponds to the end rotation of the cantilever beam in the force diagram shown in Figure 17. This can be expressed as:

$$\theta_t - \theta_b = f(D_t, d_b, d_t, P_b, P_t, V, M) \tag{32}$$

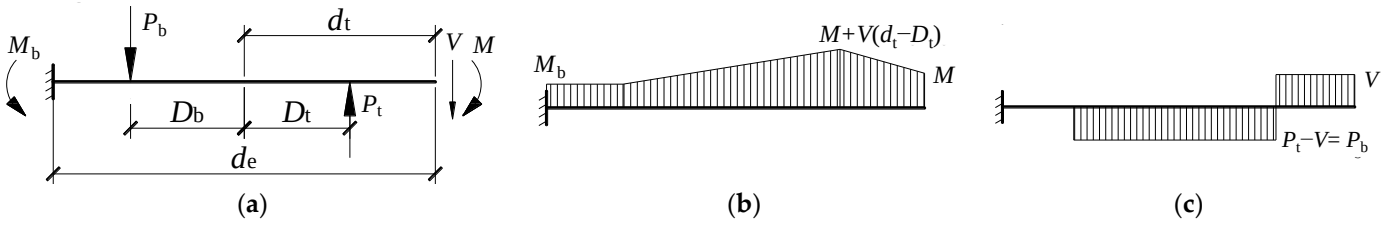


Figure 17. Force diagram and internal force distribution of a cantilever beam. (**a**) Force diagram; (**b**) bending moment diagram; (**c**) shear force diagram.

When the embedded column is in the elastic stage, the end rotation can be directly obtained using structural mechanics methods:

$$\theta_t - \theta_b = \frac{Md_e}{EI} + \frac{Vd_e^2}{2EI} + \frac{P_b(d_e - d_t - D_b)^2}{2EI} - \frac{P_t(d_e - d_t + D_t)^2}{2EI} \tag{33}$$

If the plastic stage is reached, the end rotation can be obtained by integrating the more general section curvature along the length of the beam:

$$\theta_t - \theta_b = \int_0^{d_e} \chi(x)dx \tag{34}$$

Assuming that the section material exhibits ideal elastic–plastic behaviour, the relationship between the moment and curvature of the H-beam section is as follows:

$$\begin{aligned} M = EI\chi - EI_1\left[1 - \left(\frac{\chi_{y,f}}{\chi}\right)^3\right]\chi \cdot H\left(\chi - \chi_{y,f}\right) + M_{y1}\left[1 - \left(\frac{\chi_{y,f}}{\chi}\right)^2\right] \cdot H\left(\chi - \chi_{y,f}\right) \\ + EI_2\left[1 - \left(\frac{\chi_{y,w}}{\chi}\right)^3\right]\chi \cdot H(\chi - \chi_{y,w}) - M_{y2}\left[1 - \left(\frac{\chi_{y,w}}{\chi}\right)^2\right] \cdot H(\chi - \chi_{y,w}) \end{aligned} \tag{35}$$

In which $\chi_{y,f} = 2\varepsilon_y/h_c$ and $\chi_{y,w} = 2\varepsilon_y/(h_c - 2t_f)$, which correspond to the section curvature when the outermost fibres of the flange and web enter the plastic state, respectively; and ε_y is the yield strain. The values of I, I_1, I_2, M_{y1}, and M_{y2} are as follows:

$$\begin{aligned} I = I_1 - I_2,\ I_1 = \tfrac{b_f h_c^3}{12},\ I_2 = \tfrac{(b_f - t_w)(h_c - 2t_f)^3}{12}, \\ M_{y1} = \tfrac{b_f f_y h_c^2}{4},\ M_{y2} = \tfrac{(b_f - t_w) f_y (h_c - 2t_f)^2}{4} \end{aligned} \tag{36}$$

For a cantilever beam with a length of L and an end moment of M_e, using Equation (34) and substituting the moment-curvature relationship expressed in Equation (35), the end rotation is calculated as:

$$\theta(M_e, L) = \int_0^L \chi(x)dx = \chi_e L - \int_0^{\chi_e} x d\chi = \chi_e L - \frac{L}{M_e}\int_0^{\chi_e} M d\chi \tag{37}$$

in which:

$$\begin{aligned}\int_0^{\chi_e} Md\chi = \frac{EI}{2}\chi_e^2 - EI_1\left(\frac{\chi_e^2}{2} + \frac{\chi_{y,f}^3}{\chi_e} - \frac{3}{2}\chi_{y,f}^2\right)H\left(\chi_e - \chi_{y,f}\right) + M_{y1}\frac{\left(\chi_e - \chi_{y,f}\right)^2}{\chi_e}H\left(\chi_e - \chi_{y,f}\right)\\ +EI_2\left(\frac{\chi_e^2}{2} + \frac{\chi_{y,w}^3}{\chi_e} - \frac{3}{2}\chi_{y,w}^2\right)H(\chi_e - \chi_{y,w}) - M_{y2}\frac{(\chi_e - \chi_{y,w})^2}{\chi_e}H(\chi_e - \chi_{y,w})\end{aligned} \tag{38}$$

in which χ_e is the curvature at the fixed end of the beam.

Finally, the moment diagram shown in Figure 17 consists of three linear segments. The contributions of three segments can be calculated separately and then superimposed. The rotation caused by each linearly varying segment can be equated to the difference in end rotations of two cantilever beams. Therefore, the relative rotation between the top and bottom ends of the embedded column can finally be expressed as follows:

$$\begin{aligned}\theta_t - \theta_b = \chi(M_b)(d_e - d_t - D_b)\\ +\theta\left(M + V(d_t - D_t), \frac{M+V(d_t-D_t)}{P_b}\right) - \theta\left(M_b, \frac{M_b}{P_b}\right)\\ +\theta(M + V(d_t - D_t), L_c + d_t - D_t) - \theta(M, L_c)\end{aligned} \tag{39}$$

The difference in rotation between segments III and II, i.e., $\theta_b - \theta_0$, is the shear deformation, which is equal to the deformation over the length $D_t + D_b$ under the shear force P_b:

$$\theta_b - \theta_0 = f(P_b, D_b, D_t) \tag{40}$$

Considering the ideal elastoplastic behaviour with shear deformation of the section, it can be expressed as:

$$\theta_b - \theta_0 = \begin{cases} \frac{P_b(D_b+D_t)}{GA_w} & P_b < f_{yv}A_w \\ \geq \frac{f_{yv}(D_b+D_t)}{G} & P_b = f_{yv}A_w \end{cases} \tag{41}$$

in which A_w is the column web area, f_{yv} is the yield shear stress, and G is the shear modulus.

In summary, the equation groups consisting of Equations (20), (21), (28), (29), (31), (39), and (41) (where Equations (28) and (29) each include two separate equations) can be solved to obtain the nine unknowns: θ_t, θ_0, θ_b, dt, D_t, D_b, M_b, P_t, and P_b. Due to the complexity of the equation groups, it is necessary to use the numerical iterative method.

4.4. Solution of Response

To obtain the moment–rotation curve of the ECB, the equation groups mentioned above can be solved using the flowchart shown in Figure 18:

1. First, an arbitrary value of θ_t is given, assuming that θ_t is known;
2. The initial values of θ_b and θ_0 are given and the shear and bending deformations are temporarily ignored, assuming $\theta_b = \theta_0 = \theta_t$;
3. Obtain M_b from Equation (31);
4. The initial value of d_t is given. Assuming that all components ccc are in the elastic stage, the value of d_t can be obtained by simultaneously solving Equations (20), (21), (28), and (29), i.e., Equation (42);

$$d_t = \frac{M_b + \frac{1}{6}k_e\theta_0 d_e^2(2d_e + 3L_c)}{\frac{1}{2}k_e\theta_0 d_e(d_e + 2L_c)} \tag{42}$$

5. The initial values of D_t and D_b are given. Assuming that all components ccc are in the elastic stage, it can be obtained that $D_t = 2d_t/3$ and $D_b = 2d_b/3$;
6. Calculate P_t and P_b by Equation (28);
7. Calculate new values of D_t and D_b by Equation (29), denoted as $D_{t,temp}$ and $D_{b,temp}$;
8. If $D_t \neq D_{t,temp}$ or $D_b \neq D_{b,temp}$, set $D_t = D_{t,temp}$ and $D_b = D_{b,temp}$, and repeat steps 6 and 7; if $D_t = D_{t,temp}$ and $D_b = D_{b,temp}$, calculate M by Equation (21);

9. If M does not satisfy Equation (20), calculate a new value of d_t by Equation (43) (in which k represents the lateral stiffness of the concrete on the column side corresponding to the current deformation and can be obtained by Equations (44) and (45)), denoted as $d_{t,temp}$. Set $d_t = d_{t,temp}$, then repeat steps 5 to 8; if M satisfies Equation (20), calculate new values of θ_b and θ_0 by Equations (39) and (41), denoted as $\theta_{b,temp}$ and $\theta_{0,temp}$;

$$d_{t,temp} = d_t + \frac{M/L_c - P_t + P_b}{k \cdot \theta_0} \tag{43}$$

$$k = k_t + k_b \tag{44}$$

$$\begin{aligned} k_j = k_1 d_j &+ \sum_{i=1}^{n} (k_{i+1} - k_i)(D_j - D_{i,0}) \cdot H(D_j - D_{i,0}) \\ &+ \sum_{i=1}^{n} (k_{i+1} - k_i)(d_j - D_j) \cdot H(D_j - D_{i,j}) \\ &+ \sum_{i=1}^{n} (k_{i+1} - k_i)(d_j - D_{i,j}) \cdot H(-D_j + D_{i,j}) \cdot H(d_j - D_{i,j}) \end{aligned} \tag{45}$$

10. If $\theta_b \neq \theta_{b,temp}$ or $\theta_0 \neq \theta_{0,temp}$, set $\theta_b = \theta_{b,temp}$ or $\theta_0 = \theta_{0,temp}$, and repeat steps 4 to 9; if $\theta_b = \theta_{b,temp}$ and $\theta_0 = \theta_{0,temp}$, it indicates that all equations have been satisfied, and a point (θ_t, M) on the moment–rotation curve is obtained;
11. Gradually increase θ_t and repeat the above steps to solve for several points and obtain the whole process moment–rotation curve. The precision of the moment–rotation curve depends on the precision in describing the component behaviour and the magnitude of the θ_t increment given during the solution process.

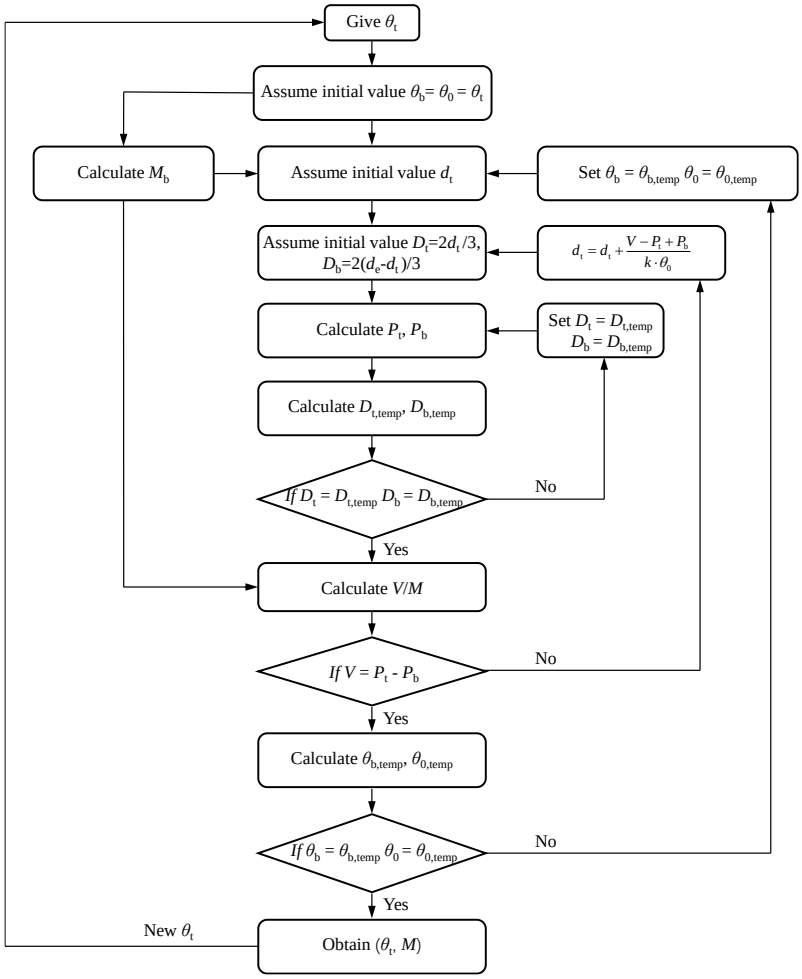


Figure 18. Flowchart for obtaining the moment–rotation curve of the ECB.

In the above flowchart, the determination of each point (θ_t, M) involves three rounds of iterative calculations. Although it appears complex, each iteration round has a clear initial value selection recommendation and iteration direction with good convergence, eliminating the need for repeated trial calculations. Consequently, it has good feasibility, along with fast convergence speed.

5. Solution of Full-Range M-θ curve—A FE Method

Section 4 presents a simplified iterative solution method for the component model of the ECB proposed in this paper. In this method, the embedded column is equivalently represented by three rigid segments, and the bending and shear deformations of the embedded column are concentrated in the relative rotations between the rigid segments. With the aid of FE software, the embedded column can be directly modelled by beam elements that consider both bending and shear deformations, allowing for a more accurate consideration of the deformations of the embedded column. Additionally, this simplified FE model based on the component method can be used not only for analysing joint behaviour but also for structural advanced analysis of frame structures, to consider the influence of joint behaviour on structural response [32,50].

This study employs the ABAQUS 2020 FE software to establish a simplified FE model based on the component method, as illustrated in Figure 19. The steel column is modelled by planar beam elements (B21), while the base plate is represented by beam elements with a very high elastic modulus, treated as equivalent rigid elements. The reason for using beam elements instead of rigid elements to represent the base plate is that it allows modelling the base plate and the steel column within the same part, eliminating the need to define constraints between them and enhancing modelling efficiency. The remaining components, including the components ccc, ccb, csb and the anchor bolt-base plate equivalent T-stub, are all modelled using Connector elements with axial behaviour. Apart from Connector elements, truss elements or spring elements can also be used, with the specific choice depending on the convenience of modelling and element property setting. Connector elements are selected because they can easily represent very complex axial nonlinear behaviour. One end of the Connector element is coupled with the node of the beam element, while the other end is fixed.

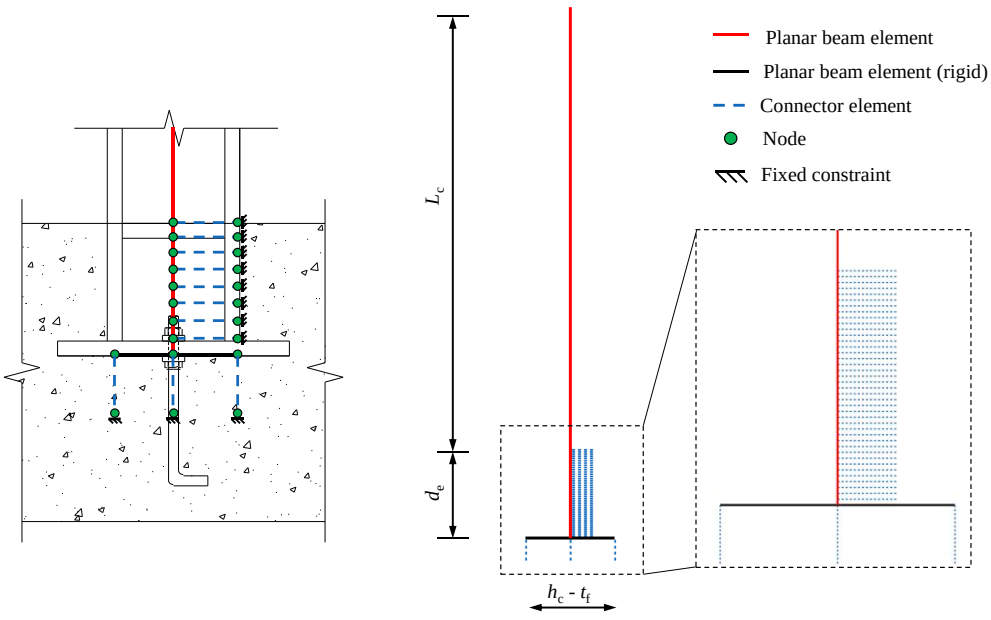


Figure 19. Simplified FE model based on the component method. (**a**) Schematic diagram; (**b**) FE model.

In the direction of embedded depth, the horizontal Connector elements need to reach a certain number. Trial calculations indicate that dividing the embedded column into 40 segments on average and setting 41 Connector elements can meet this requirement. Further increasing the number does not affect the moment–rotation curve. In addition, the load–displacement relationship of the first and last Connector elements is 1/2 of that of the middle Connector elements, to accurately reflect the uniformly distributed compressive stress. The embedded column segment meshes into 40 elements, the cantilever segment of the steel column into 100 elements, and the base plate into only 2 elements. Hence, the model comprises 142 beam elements and 44 Connector elements. Mesh convergence analysis indicated that further increasing the number of elements did not affect the results.

6. Model Validation

Studies [2,51] have conducted experimental investigations of the bending performance of embedded H-steel column bases in the strong axis direction and presented the moment–rotation curves at the interface between the steel column and the foundation surface. The test setups are shown in Figure 20, with a total of eight specimens. Table 2 summarizes the basic dimensions and material information for all tested specimens, and more detailed information can be found in the references [2,51]. In [2], the embedded depth ratios of the 5 specimens vary between 1.0 and 1.8, and different levels of axial force are applied to the steel columns. In [51], the embedded depth ratios of the 3 specimens range from 0.5 to 1.5, and based on a validated refined solid FE model, moment–rotation curves are provided for embedded depth ratios between 2.0 and 4.0. These FE results are also used to verify the applicability of the theoretical model for column bases with larger embedded depths, and the relevant FE model parameters are listed in Table 2.

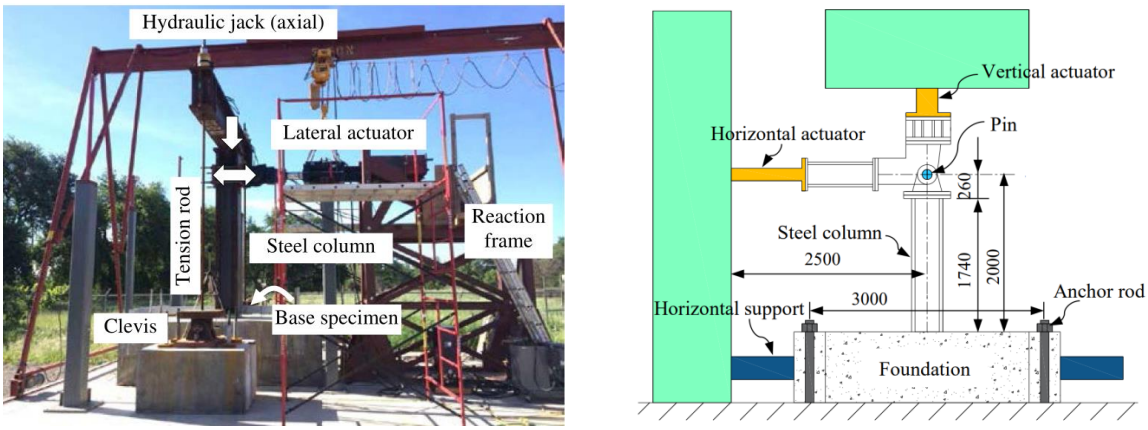


Figure 20. Experimental tests. (**a**) Reference [2] (Reproduced with permission from [2], ASCE, 2017); (**b**) Reference [51].

Figure 21 compares the moment–rotation curves obtained from the experimental and theoretical models. Since the tests conducted in [20] are hysteretic, the curves labelled TEST(+) and TEST(−) in the figure represent the moment–rotation skeleton curves in the positive and negative directions, respectively. The curve labelled TEST represents the moment–rotation curve obtained from a monotonic loading test. The predicted curves labelled MODEL and FEM-S are obtained, respectively, from the simplified iterative solution method presented in Section 4 and the simplified FE model based on the component method established in Section 5. Overall, the predicted curves agree well with the experimental curves, demonstrating similar initial stiffness, gradually developing plasticity, and ultimate failure modes. In the initial stage of loading, the moment increases linearly with the rotation. As the concrete in punching shear above the base plate and the concrete in compression on the column side gradually approach failure, the stiffness begins to decrease.

After the base plate reaches its moment resistance, the increase at the moment resistance of the ECB is solely contributed by the horizontal moment-resisting mechanism showing that the secant stiffness of the ECB gradually decreases to zero and the ECB reaches its peak moment resistance. Subsequently, due to the progressive failure of the concrete in compression on the column side, the moment resistance decreases, and the moment–rotation curve enters the descending phase.

Table 2. Basic dimensions and material information of the specimens.

	No.	Name	Column Size (mm)	Base Plate Size (mm)	Foundation Width (mm)	Material Strength (MPa)		Embedded Depth (mm)	Exposed Height (mm)	Axial Force * (kN)	Literature
			$h_c \times b_c \times t_w \times t_f$	$h_p \times b_p \times t_p$	B_c	f_y	f_c	d_e	L_c	P	
Tests	1	Test1	455 × 419 × 42 × 68	762 × 762 × 51	1830	345	29.2	559	2840	445	Grilli et al. [20]
	2	Test2	567 × 305 × 39 × 70	864 × 711 × 51	1830	345	29.2	559	2840	445	
	3	Test3	455 × 419 × 42 × 68	762 × 762 × 51	1830	345	29.2	813	3100	0	
	4	Test4	455 × 419 × 42 × 68	762 × 762 × 51	1830	345	29.2	813	3100	445	
	5	Test5	455 × 419 × 42 × 68	762 × 762 × 51	1830	345	29.2	813	3100	−667	
FE models	6	S-0.5	400 × 400 × 30 × 45	600 × 450 × 45	900	381	26.1	200	2000	0	Xu [51]
	7	S-1.0	400 × 400 × 30 × 45	600 × 450 × 45	900	381	26.1	400	2000	0	
	8	S-1.5	400 × 400 × 30 × 45	600 × 450 × 45	900	381	26.1	600	2000	0	
	9	S-2.0	400 × 400 × 30 × 45	600 × 450 × 45	900	381	26.1	800	2000	0	
	10	S-2.5	400 × 400 × 30 × 45	600 × 450 × 45	900	381	26.1	1000	2000	0	
	11	S-3.0	400 × 400 × 30 × 45	600 × 450 × 45	900	381	26.1	1200	2000	0	
	12	S-3.5	400 × 400 × 30 × 45	600 × 450 × 45	900	381	26.1	1400	2000	0	
	13	S-4.0	400 × 400 × 30 × 45	600 × 450 × 45	900	381	26.1	1600	2000	0	

* Axial force is considered positive when it is compressive.

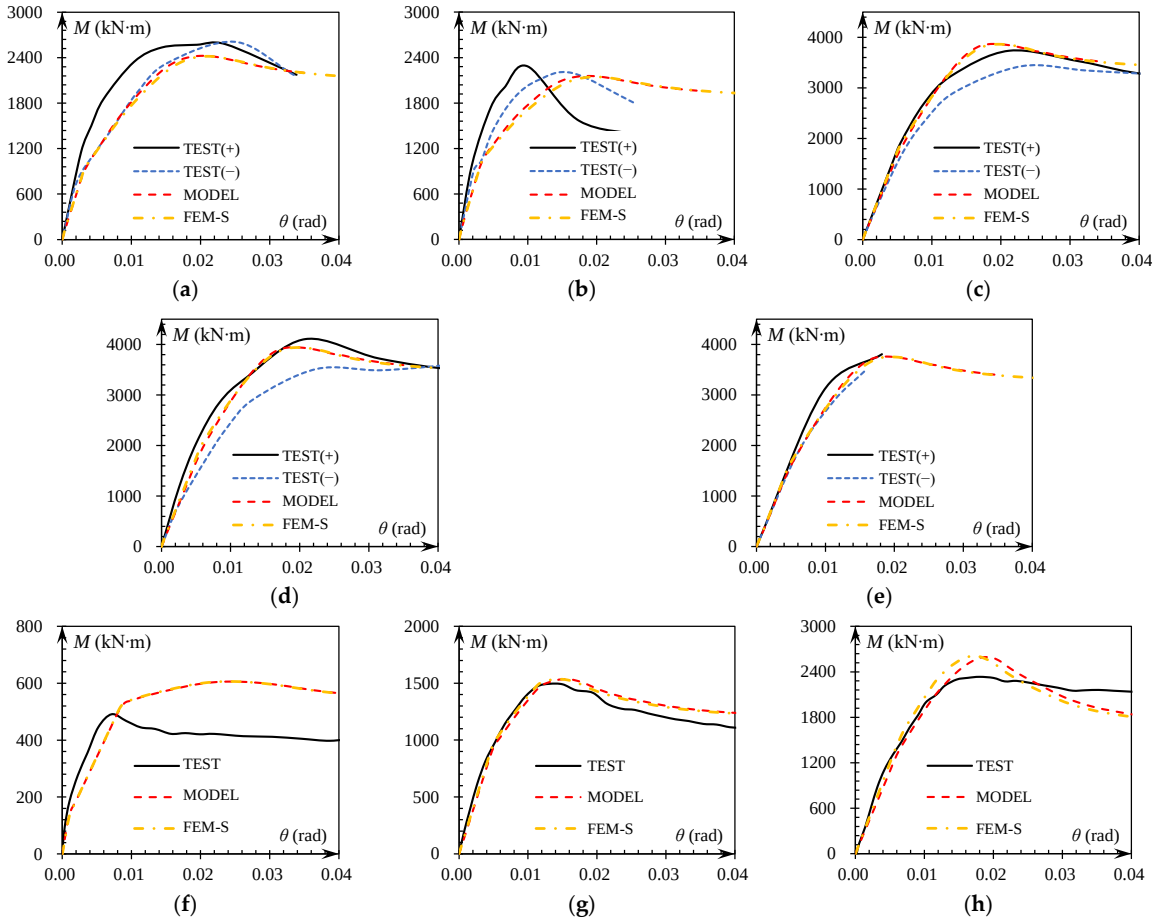


Figure 21. Comparison of moment–rotation curves obtained from component model and tests. (**a**) Test1; (**b**) Test2; (**c**) Test3; (**d**) Test4; (**e**) Test5; (**f**) S-0.5; (**g**) S-1.0; (**h**) S-1.5.

The simplified FE model based on the component method can be regarded as an accurate solution to the component model. It can be observed that the curves obtained from the simplified iterative solution method and the simplified FE model have a high degree of coincidence. The slight difference is caused by the simplification of the deformation of the embedded column segment in the simplified solution iterative method, which assumes that the deformation of the embedded column follows a trilinear pattern. Compared to other specimens, the specimen corresponding to Figure 21h has both a relatively weak cross-section and a larger embedded depth, resulting in significant deformation of the embedded column. Consequently, the differences between the results of MODEL and FEM-S begin to manifest.

The initial stiffness (K_{MODEL} and $K_{\text{FEM-S}}$) and moment resistance (M_{MODEL} and $M_{\text{FEM-S}}$) predicted by the component model are summarized in Table 3 and compared with the experimental results. The model provides a relatively accurate prediction of the initial stiffness. The ratio of stiffness obtained from the FE model based on the component method to the experimental results ($K_{\text{FEM-S}}/K_{\text{TEST}}$) for the eight specimens ranges from 0.88 to 1.13, with a mean value and coefficient of variation (Cov) of 0.98 and 0.08, respectively. The predicted moment resistance also agrees well with the experimental results. The ratio $M_{\text{FEM-S}}/M_{\text{TEST}}$ ranges from 0.93 to 1.23, with a mean value and Cov of 1.05 and 0.09, respectively.

Table 3. Comparison of the results obtained from component models and tests.

Specimens	TEST		MODEL				FEM-S				MODEL/FEM-S	
	K_{TEST} *	M_{TEST} *	K_{MODEL}	M_{MODEL}	$\frac{K_{\text{MODEL}}}{K_{\text{TEST}}}$	$\frac{M_{\text{MODEL}}}{M_{\text{TEST}}}$	$K_{\text{FEM-S}}$	$M_{\text{FEM-S}}$	$\frac{K_{\text{FEM-S}}}{K_{\text{TEST}}}$	$\frac{M_{\text{FEM-S}}}{M_{\text{TEST}}}$	$\frac{K_{\text{MODEL}}}{K_{\text{FEM-S}}}$	$\frac{M_{\text{MODEL}}}{M_{\text{FEM-S}}}$
Test1	3.23	2596	3.04	2418	0.94	0.93	3.07	2425	0.95	0.93	0.99	1.00
Test2	3.84	2246	3.35	2147	0.87	0.96	3.38	2156	0.88	0.96	0.99	1.00
Test3	3.07	3593	3.32	3872	1.08	1.08	3.47	3865	1.13	1.08	0.96	1.00
Test4	3.38	3868	3.43	3945	1.01	1.02	3.62	3938	1.07	1.02	0.95	1.00
Test5	3.25	3632	3.15	3765	0.97	1.04	3.24	3756	1.00	1.03	0.97	1.00
S-0.5	0.97	491	0.91	606	0.94	1.23	0.92	606	0.95	1.23	0.99	1.00
S-1.0	2.10	1495	1.90	1534	0.90	1.03	1.96	1536	0.93	1.03	0.97	1.00
S-1.5	2.40	2334	2.17	2595	0.90	1.11	2.39	2612	1.00	1.12	0.91	0.99
Mean	—	—	—	—	0.95	1.05	—	—	0.98	1.05	0.97	1.00
Cov	—	—	—	—	0.07	0.09	—	—	0.08	0.09	0.03	0.003

* The unit for K is 10^5 kN·m/rad, and the unit for M is kN·m. K_{TEST} and M_{TEST} for Test1 to Test5 represent the average values of results in two directions.

Figure 22 compares the moment–rotation curves obtained from the validated refined solid FE models (FEM) and theoretical prediction curves (MODEL and FEM-S) for five deep ECBs with embedded depth ratios varying from 2.0 to 4.0. The stiffness and moment resistance are summarized in Table 4. It can be observed that the simplified FE model based on the component method also achieves results that are highly consistent with those of the refined FE model. However, it is important to note that as the embedded depth increases, differences begin to emerge between the results of the simplified method and the simplified FE results. The rotational stiffness obtained by the former is lower than that of the latter, and when the embedded depth ratio is 4.0, the ratio is only 0.66. As mentioned earlier, the simplified solution process approximates the embedded column as three rigid segments, concentrating bending deformation at the resultant force point near the foundation surface. This simplification leads to an overestimation of the rotation at the top of the embedded column, especially under conditions of deeper embedded depth and more pronounced bending deformation. However, although the simplified solution method has a greater impact on stiffness when the embedded depth is deeper, it has a smaller impact on moment resistance. When the embedded depth ratio is 4.0, the ratio of moment resistance obtained by the two methods differs by only 5%.

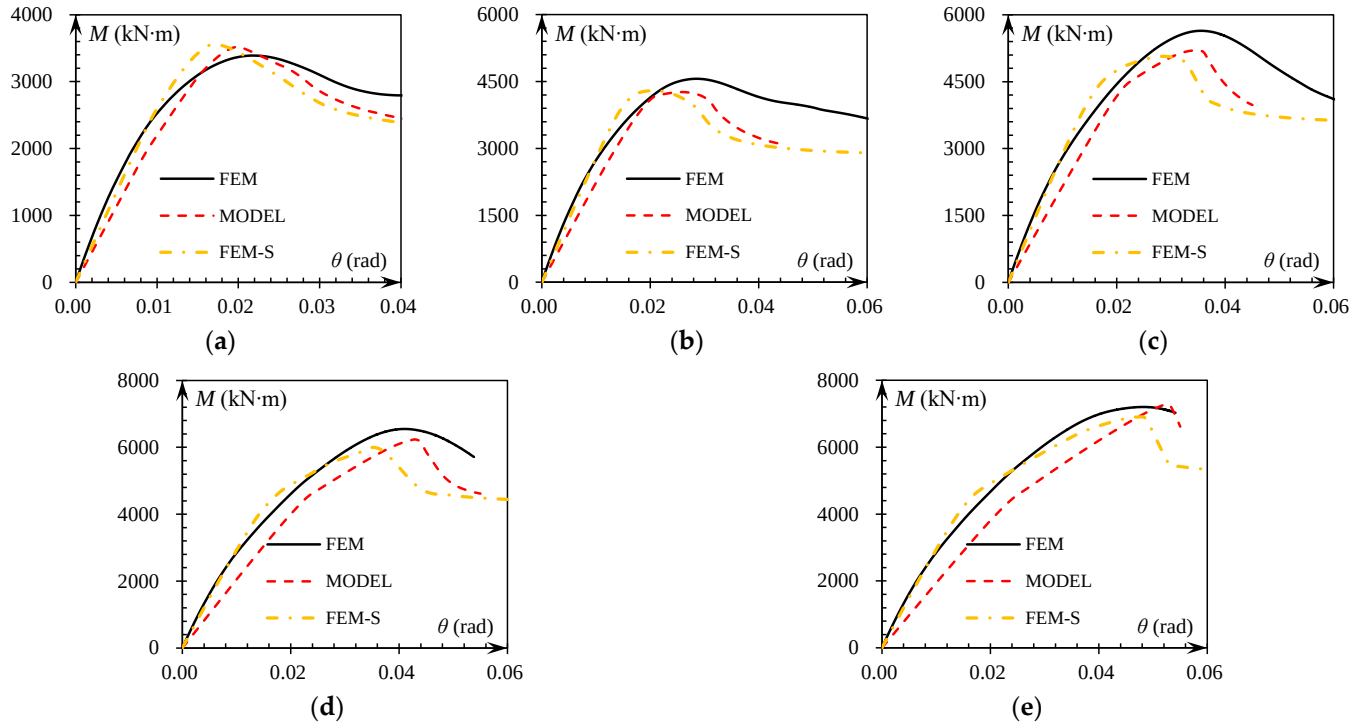


Figure 22. Comparison of the results obtained from component models and refined solid FE models. (**a**) S-2.0; (**b**) S-2.5; (**c**) S-3.0; (**d**) S-3.5; (**e**) S-4.0.

Table 4. Comparison of the results obtained from component models and refined solid FE models.

Specimens	FEM		MODEL				FEM-S				MODEL/FEM-S	
	K_{FEM} *	M_{FEM} *	K_{MODEL}	M_{MODEL}	$\frac{K_{MODEL}}{K_{FEM}}$	$\frac{M_{MODEL}}{M_{FEM}}$	K_{FEM-S}	M_{FEM-S}	$\frac{K_{FEM-S}}{K_{FEM}}$	$\frac{M_{FEM-S}}{M_{FEM}}$	$\frac{K_{MODEL}}{K_{FEM-S}}$	$\frac{M_{MODEL}}{M_{FEM-S}}$
S-2.0	2.85	3391	2.26	3524	0.79	1.04	2.65	3552	0.93	1.05	0.85	0.99
S-2.5	2.94	4560	2.24	4262	0.76	0.93	2.87	4296	0.98	0.94	0.78	0.99
S-3.0	2.99	5644	2.20	5197	0.74	0.92	2.98	5065	1.00	0.90	0.74	1.03
S-3.5	3.02	6548	2.10	6237	0.70	0.95	3.04	5940	1.01	0.91	0.69	1.05
S-4.0	3.02	7205	2.00	7270	0.66	1.01	3.07	6898	1.02	0.96	0.65	1.05
Mean	—	—	—	—	0.73	0.97	—	—	0.99	0.95	0.74	1.02
Cov	—	—	—	—	0.06	0.05	—	—	0.03	0.06	0.09	0.03

* The unit for K is 10^5 kN·m/rad, and the unit for M is kN·m.

7. Conclusions

The component model of the ECB constructed in this paper is aimed at predicting the stiffness, moment resistance, and even the full-range moment–rotation behaviour of the ECB. The characteristics of this model and the contributions of this paper include the following:

(1) Based on the moment-resisting mechanism of the ECB, key components such as the embedded column, concrete in compression on the column side, concrete in compression beneath the base plate, concrete in punching shear above the base plate, and anchor bolts were identified. Among these, the embedded column was simplified as a Timoshenko beam considering bending and shear deformations, while the remaining components were simplified as springs, and methods for determining their uniaxial behaviour were established. Ultimately, a simplified mechanical model for predicting the flexural behaviour of the ECB, referred to as the component model, was established.

(2) To solve the component model, a method for establishing a simplified FE model based on the component method is presented. This method can be regarded as an FE

solution for the component model and is capable of providing accurate solutions. Additionally, a simplified iterative solution method is proposed, which is characterized by the simplification of the Timoshenko beam representing the embedded column into three rigid segments based on the force and deformation characteristics of the embedded column. Relative rotation can occur between these segments to collectively represent the bending and shear deformations of the embedded column. Ultimately, based on equilibrium equations, deformation compatibility equations, and component constitutive relationships, a system of equations capable of describing this component system is established, and the iterative solution method is provided.

The component model was applied to eight experimental specimens and five refined solid FE numerical models of ECBs for H-steel columns, demonstrating good consistency in the full-range moment–rotation behaviour, including stiffness and moment resistance. The mean values of the ratios of the predictions by the simplified FE model based on the component method to the experimental results were 0.98 and 1.05, respectively, corresponding to stiffness and moment resistance. Additionally, the simplified iterative solution method proposed in this paper also achieved good predictions of moment resistance. However, in cases with larger embedded depth, it underestimated the stiffness. The reason is that during the simplified process of the component model, it was assumed that the deformation of the embedded column followed a trilinear mode, concentrating the bending deformation at the resultant force point of upper bearing stress, which led to an overestimation of the rotation of the steel column at the foundation surface.

Author Contributions: Conceptualization, J.L.; methodology, J.L.; software, X.X.; validation, X.X.; formal analysis, X.X.; investigation, X.X.; resources, X.X.; data curation, X.X.; writing—original draft preparation, X.X.; writing—review and editing, X.X.; visualization, S.Y.; supervision, S.Y. All authors have read and agreed to the published version of the manuscript.

Funding: This research was funded by the National Natural Science Foundation of China, grant number 52178152.

Data Availability Statement: The data presented in this study are available on request from the corresponding author.

Conflicts of Interest: The authors declare no conflicts of interest.

References

1. Sato, A.; Kitagawa, H. Seismic Design Procedure for Low-Rise Cold-Formed Steel-Special Bolted Moment Frames. *Appl. Sci.* **2024**, *14*, 4520. [CrossRef]
2. Grilli, D.; Jones, R.; Kanvinde, A. Seismic Performance of Embedded Column Base Connections Subjected to Axial And Lateral Loads. *J. Struct. Eng.* **2017**, *143*, 04017010. [CrossRef]
3. Inamasu, H.; Kanvinde, A.M.; Lignos, D.G. Seismic Stability of Wide-Flange Steel Columns Interacting with Embedded Column Base Connections. *J. Struct. Eng.* **2019**, *145*, 04019151. [CrossRef]
4. Inamasu, H.; Lignos, D.G. Seismic Performance of Steel Columns Interacting with Embedded Column Bases While Exhibiting Inelastic Deformations. *Eng. Struct.* **2022**, *251*, 113381. [CrossRef]
5. Morino, S.; Kawaguchi, J.; Tsuji, A. Strength and Stiffness of CFT Semi-Embedded Type Column Base. In Proceedings of the ASSCCA 2003, Sydney, Australia, 22–25 June 2003.
6. Cui, Y.; Nagae, T.; Nakashima, M. Hysteretic Behavior and Strength Capacity of Shallow Embedded Steel Column Bases. *J. Struct. Eng.* **2009**, *135*, 1231–1238. [CrossRef]
7. Cui, Y.; Nakashima, M. Hysteretic Behavior and Strength Capacity of Shallow Embedded Steel Column Bases with SFRCC Slab. *Earthq. Eng. Struct. Dyn.* **2011**, *40*, 1495–1513. [CrossRef]
8. Hanks, K.N.; Richards, P.W. Experimental Performance of Block-Out Connections at the Base of Steel Moment Frames. *J. Struct. Eng.* **2019**, *145*, 04019057. [CrossRef]
9. Pecce, M.; Rossi, F. The Non-Linear Model of Embedded Steel–Concrete Composite Column Bases. *Eng. Struct.* **2013**, *46*, 247–263. [CrossRef]
10. Hetényi, M. *Beams on Elastic Foundation: Theory with Applications in the Fields of Civil and Mechanical Engineering*; University of Michigan Press: Ann Arbor, MI, USA, 1946.
11. Richards, P.W.; Barnwell, N.V.; Tryon, J.E.; Sadler, A.L. Flexural Strength and Stiffness of Block-Out Connections for Steel Columns. *Eng. Struct.* **2018**, *173*, 404–415. [CrossRef]

12. Zhao, X.Z.; Xu, X.X.; Yan, S. Stiffness model for embedded steel column bases considering the effects of axial force and constraint of base plate. *J. Harbin Inst. Technol.* **2024**, *56*, 18–27.
13. Rodas, P.T.; Zareian, F.; Kanvinde, A. Rotational Stiffness of Deep Embedded Column–Base Connections. *J. Struct. Eng.* **2017**, *143*, 04017064. [CrossRef]
14. Shahrooz, B.M.; Remmetter, M.E.; Qin, F. Seismic Design and Performance of Composite Coupled walls. *J. Struct. Eng.* **1993**, *119*, 3291–3309. [CrossRef]
15. Marcakis, K.; Mitchell, D. Precast Concrete Connections with Embedded Steel Members. *PCI J.* **1980**, *25*, 88–116. [CrossRef]
16. *Recommendations for Design of Connections in Steel Structures*; Architectural Institute of Japan: Tokyo, Japan, 2012.
17. *ANSI/AISC 341–16*; Seismic Provisions for Structural Steel Buildings. American Institute of Steel Construction: Chicago, IL, USA, 2016.
18. *GB 50017-2017*; Standard for Design of Steel Structures. China Architecture & Building Press: Beijing, China, 2017.
19. Pertold, J.; Xiao, R.Y.; Wald, F. Embedded Steel Column Bases: II. Design Model Proposal. *J. Constr. Steel Res.* **2000**, *56*, 271–286. [CrossRef]
20. Grilli, D.A.; Kanvinde, A.M. Embedded Column Base Connections Subjected to Seismic Loads: Strength Model. *J. Constr. Steel Res.* **2017**, *129*, 240–249. [CrossRef]
21. Ma, R.; Xia, J.; Chang, H.; Xu, B. A Component-Based Model for Novel Modular Connections with Inbuild Component. *Appl. Sci.* **2021**, *11*, 10503. [CrossRef]
22. Zoetemaijer, P. A Design Method for the Tension Side of Statically Loaded Bolted Beam-to-Column Connections. *Heron* **1974**, *20*, 1–59.
23. Packer, J.A.; Morris, L.J. A Limit State Design Method for the Tension Region of Bolted Beam-Column Connections. *Struct. Eng.* **1977**, *55*, 446–458.
24. Yee, Y.L.; Melchers, R. Moment-Rotation Curves for Bolted Connections. *J. Struct. Eng.* **1986**, *112*, 615–635. [CrossRef]
25. Jaspart, J.P.; Weynand, K.; Steenhuis, M. The Stiffness Model of Revised Annex J of Eurocode 3. In Proceedings of the 3rd International Workshop on Connections in Steel Structures, Trento, Italy, 29–31 May 1995.
26. Faella, C.; Piluso, V.; Rizzano, G. *Structural Steel Semirigid Connections: Theory, Design and Software*; CRC Press: London, UK, 2000.
27. *EN 1993-1-8*; Eurocode 3: Design of Steel Structures–Part 1–8: Design of Joints. European Committee for Standardization: Brussels, Belgium, 2005.
28. Jaspart, J.P.; Vandegans, D. Application of the component method to column bases. *J. Constr. Steel Res.* **1998**, *48*, 89–106. [CrossRef]
29. Zhu, C.; Rasmussen, K.J.R.; Yan, S. Generalised Component Model for Structural Steel Joints. *J. Constr. Steel Res.* **2019**, *153*, 330–342. [CrossRef]
30. Wan, W.; Yan, S.; Zhang, H.; Rasmussen, K.J.R. A Generalised Component Method for Bolted Angle Connections. *J. Constr. Steel Res.* **2022**, *198*, 107530. [CrossRef]
31. Latour, M.; Rizzano, G. A Theoretical Model for Predicting the Rotational Capacity of Steel Base Joints. *J. Constr. Steel Res.* **2013**, *91*, 89–99. [CrossRef]
32. Yan, S.; Rasmussen, K.J.R. Generalised Component Method-Based Finite Element Analysis of Steel Frames. *J. Constr. Steel Res.* **2021**, *187*, 106949. [CrossRef]
33. Lyu, J.; Yan, S.; He, S.; Zhao, X.Z.; Rasmussen, K. Mechanical Model for the Full Range Behavior of Bolted T-Stubs. *J. Constr. Steel Res.* **2023**, *200*, 107652. [CrossRef]
34. Francavilla, A.B.; Latour, M.; Piluso, V.; Rizzano, G. Bolted T-Stubs: A Refined Model for Flange and Bolt Fracture Modes. *Steel Compos. Struct.* **2016**, *20*, 267–293. [CrossRef]
35. Francavilla, A.B.; Latour, M.; Rizzano, G. Ultimate Behavior of Bolted T-Stubs under Large Displacements: A Mechanical Model. *J. Constr. Steel Res.* **2022**, *195*, 107355. [CrossRef]
36. Lemonis, M.; Gantes, C. Incremental Modeling of T-Stub Connections. *J. Mech. Mater. Struct.* **2006**, *1*, 1135–1159. [CrossRef]
37. Mattock, A.H.; Gaafar, G.H. Strength of Embedded Steel Sections as Brackets. *ACI J.* **1982**, *79*, 83–93.
38. Deierlein, G.G.; Sheikh, T.M.; Yura, J.A.; Jirsa, J.O. Beam-Column Moment Connections for Composite Frames: Part 2. *J. Struct. Eng.* **1989**, *115*, 2877–2896. [CrossRef]
39. Sheikh, T.M.; Deierlein, G.G.; Yura, J.A.; Jirsa, J.O. Beam-Column Moment Connections for Composite Frames: Part 1. *J. Struct. Eng.* **1989**, *115*, 2858–2876. [CrossRef]
40. The ASCE Task Committee on Design Criteria for Composite Structures in Steel and Concrete. Guidelines for design of joints between steel beams and reinforced concrete columns. *J. Struct. Div. ASCE* **1994**, *120*, 2330–2357. [CrossRef]
41. *GB 50010—2010*; Code for Design of Concrete Structures. China Architecture & Building Press: Beijing, China, 2010.
42. McKenna, F. Object Oriented Finite Element Programming: Frameworks for Analysis, Algorithms and Parallel Computing. Ph.D. Thesis, University of California, Berkeley, Berkeley, CA, USA, 1997.
43. Stockwell, F.W. Preliminary Base Plate Selection. *Eng. J. AISC* **1975**, *21*, 92–99. [CrossRef]
44. Steenhuis, C.M.; Wald, F.; Sokol, Z.; Stark, J. Concrete in compression and base plate in bending. *Heron* **2008**, *53*, 109–126.
45. *ACI 318-19*; Building Code Requirements for Structural Concrete (ACI 318-19) and Commentary (ACI 318R-19). American Concrete Institute: Farmington Hills, MI, USA, 2019.
46. Latour, M.; Piluso, V.; Rizzano, G. Rotational Behaviour of Column Base Plate Connections: Experimental Analysis and Modelling. *Eng. Struct.* **2014**, *68*, 14–23. [CrossRef]

47. Abidelah, A.; Bouchaïr, A.; Kerdal, D.E. Experimental and Analytical Behavior of Bolted End-plate Connections with or without Stiffeners. *J. Constr. Steel Res.* **2012**, *76*, 13–27. [CrossRef]
48. Chen, X.S.; Shi, G. Experimental Study of End-plate Joints with Box Columns. *J. Constr. Steel Res.* **2018**, *143*, 307–319. [CrossRef]
49. Zhao, X.Z.; He, S.B.; Yan, S. Full-range Behaviour of T-stubs with Various Yield Line Patterns. *J. Constr. Steel Res.* **2021**, *186*, 106919. [CrossRef]
50. Song, B.; Hassan, A.; Kanvinde, A.; Calasso, C. Probabilistic seismic performance assessment of steel moment-resisting frames considering exposed column-base plate connections with ductile anchor rods. *Earthq. Eng. Struct. Dyn.* **2023**, *52*, 3811–3834. [CrossRef]
51. Xu, X.X. Research on Flexural Performance and Theoretical Model of Embedded Column Bases. Ph.D. Thesis, Tongji University, Shanghai, China, 2023.

Disclaimer/Publisher's Note: The statements, opinions and data contained in all publications are solely those of the individual author(s) and contributor(s) and not of MDPI and/or the editor(s). MDPI and/or the editor(s) disclaim responsibility for any injury to people or property resulting from any ideas, methods, instructions or products referred to in the content.